Accepted to Phys. Fluids 10.1063/5.0122146

Bifurcations to quasiperiodicity of the torsional solutions of convection in rotating fluid spheres: Techniques and results

J. Sánchez Umbría* and M. Net†

Physics Department, Universitat Politècnica de Catalunya,

Jordi Girona Salgado 1–3, Campus Nord,

Mòdul B4, 08034 Barcelona, Spain

(Dated: September 28, 2022)

Abstract

The linear stability of the periodic and axisymmetric solutions of the convection in rotating, internally heated, and self-gravitating fluid spheres is presented. The transition to quasiperiodic flows via Neimark-Sacker bifurcations of different azimuthal wave numbers, m, is studied using matrix-free continuation and Floquet theory. Several pairs of Ekman and Prandtl numbers are considered in the region where the first bifurcation from the conduction state gives rise to the axisymmetric solutions. It is shown that the azimuthal wave numbers $m = 1$ and $m = 2$ are preferred, and that, for small Ekman and Prandtl numbers, the secondary bifurcations to different m accumulate close to the onset of convection. This study confirms some results previously found just by direct simulations. The methods presented can be applied to systems of parabolic partial differential equations with O(2) or SO(2) symmetry group, when a periodic orbit, invariant under the group, loses stability through a Neimark-Sacker bifurcation.

PACS numbers: 47.15.-x, 47.20.-k

Keywords: Rotating fluid spheres, Thermal convection, Periodic flows, Continuation, Stability, Floquet theory, Matrix-free methods.

* juan.j.sanchez@upc.edu

† marta.net@upc.edu

I. INTRODUCTION

The thermal convection in rotating, self-gravitating, internally heated fluid spheres or spherical shells is a classical problem in fluid mechanics, with clear applications to Astrophysics and Geophysics. It models the hydrodynamic behavior of the liquid or gaseous spherical objects, internal fluid cores or layers of planets or stars. The sources of internal heating can be thermonuclear reactions, as happen in the massive stars of the main sequence, or the secular cooling down of a liquid metallic core, as seems to happen, for instance, in Venus or Mars. The information obtained from such simplified models has been used to try to understand the origin of the patterns observed in the atmospheres of planets and the surface of the Sun, and the generation of magnetic fields by dynamo effect in the interior of celestial bodies.

A first simplification consists in considering a single fluid, instead of a mixture, with homogeneous properties except in the term responsible of the buoyancy forces, in which the density is considered to be proportional to the temperature. This is the so called Boussinesq approximation. In this framework the system depends on three main non-dimensional parameters, the Prandtl number, Pr, which is the ratio of the momentum to the heat diffusion and characterizes the type of fluid, the Rayleigh number, Ra, which is proportional to the amount of heat released into the fluid per unit time and measures the intensity of the buoyancy forces driving the convection, and the Ekman number, Ek, which measures the ratio of the momentum diffusion to the Coriolis force. This inertial force appears when the equations are written in a rotating frame of reference moving with the bulk of the fluid. In the case of a shell the ratio of the inner to the outer radius, $\eta = r_i/r_o$, has also to be considered. In this article some references will be made to simulations for very low η, which mimic the full sphere, but this will not be one of the parameters taken into account because it focuses on spheres. Another parameter is the Froude number, Fr, which measures the ratio of the centrifugal to the gravitational forces. It is relevant to astrophysical problems when the rotation is so large that the spherical approximation is not valid and the fluid adopts the shape of an ellipsoid in hydrostatic equilibrium (see, for instance, [1]). It will not appear in our formulation because it is very small for most planets and stars.

The values of some of the parameters in realistic conditions are extreme. Estimations of Ek for the outer Earth's core, Jupiter's atmosphere, and cold neutron stars, for instance, are of order 10^{-15}, 10^{-8}, and 10^{-10}, respectively [2, 3]. The estimated values of Pr go from moderate, $\mathcal{O}(10^{-1}) \leq \mathrm{Pr} \leq \mathcal{O}(1)$, for gases to low, $\mathcal{O}(10^{-3}) \leq \mathrm{Pr} \leq \mathcal{O}(10^{-1})$, for liquid metals. The extreme values of Ek give rise to large values of Ra. For instance, its critical value for the onset of the thermal Rossby waves, arising for moderate and large Pr, grows according to the power law $\mathrm{Ra_c} \sim \mathrm{Ek}^{-4/3}$ [4–6].

Boundary conditions must be added to close the problem. For the velocity field a common assumption is considering the flow at rest at the boundaries in the frame rotating with the walls of the fluid (non-slip boundary conditions), for example in the case of a spherical shell in contact with an inner solid core and an outer solid or plastic layer (as in the outer Earth's core, for instance). Another option is considering impenetrable walls (zero normal velocity), without tangential forces (stress-free boundary conditions). This is a first approximation of a free external surface (as in a gaseous star, for instance). For the temperature it is common to consider perfectly conducting walls at constant temperature, i.e., a Dirichlet condition. In this case the heat released to the exterior is proportional to the radial derivative of the temperature. It is also possible to enforce some kind of radiation condition with a heat flux proportional to the temperature (Robin condition) or to its fourth power (Stefan-Boltzmann law). In this article impenetrable, stress-free, and perfectly conducting boundary conditions will be used. With all the above settings there is always a solution of the Navier-Stokes and temperature equations, with the fluid being at rest in the rotating frame, and the temperature depending only on the radius. This is the so-called conduction state since the heat transport is due only to thermal conduction.

Several approaches can be used to study the fluid flows in this setup. Direct numerical simulations (DNS), performing time integration of the evolution equations for the velocity and temperature (and eventually the magnetic field), allow obtaining the fully developed flows to compute statistics or averages of global properties, pictures of the patterns of convection, and the induced magnetic fields [7–13]. Realistic values of the parameters cannot be reached because of the computational cost. The estimation in [14] for the simulation of the geodynamo at $\mathrm{Ek} = 10^{-9}$, using very efficient spectral methods, predicts that it would take 13000 days using 54000 processors to integrate a unit of the magnetic diffusion time. The lowest Ek reached in simulations without the magnetic field are, for instance, 10^{-6} with $\mathrm{Ra} = \mathcal{O}(10^{9})$ and $\mathrm{Pr} = \mathcal{O}(1)$ [15], or 10^{-8} with $\mathrm{Ra} = \mathcal{O}(10^{10})$ and $\mathrm{Pr} = \mathcal{O}(10^{-2})$ [9], although in the latter case hyperviscosity was used. Extrapolations to small Ek from the simulations for feasible values have been performed in some of the articles cited. In any case the information obtained has been useful to the knowledge of the problem. On the other side, studying the onset of convection with time evolution codes can be very inefficient since large transients are present, and the multiplicity of nearby bifurcations for low Ek can make it very tricky.

Another possibility is to study the transitions from the conduction state by means of double asymptotic limits (Ek $\ll 1$ and Pr/Ek $\gg 1$, or Ek $\ll 1$ and Pr/Ek $\ll 1$) or more recently just for Ek $\ll 1$ under a few assumptions [4, 5, 16–21]. Scaling laws for the critical Ra at the onset of convection, the frequency and the preferred azimuthal wave number of the bifurcated longitudinal waves have been obtained in this way.

A third way is to study the sequence of bifurcations from the conduction state to complex flows (quasiperiodic or temporally chaotic) using continuation techniques to find the dependence with the parameters of the solutions (steady or periodic), and checking their stability to find the subsequent transitions. This methodology based on using dynamical systems tools has been adopted here, and has been used in the past by many authors to track branches of equilibria, periodic orbits, loci of bifurcations of both objects, and even invariant tori and unstable manifolds of periodic orbits, in several problems in Fluid Mechanics; in particular in the Taylor-Couette problem [22–25], and in convection is spheres and spherical shells [26–29]. See also [30–34].

The solutions that appear when the conduction state loses stability can be classified in terms of their symmetries and temporal dependence. The system of partial differential equations (PDEs) governing the fluid is equivariant under the group $SO(2)\times Z_2$, generated by the rotations about the axis of the sphere and the equatorial reflection. Since the linearized problem about the conduction state is not self-adjoint, the first bifurcation leads generically to periodic regimes. In the most common case, first found in [4], the onset of convection gives rise to rotating azimuthal waves of a non-zero wave number, m, which are symmetric relative to the equatorial reflection. Since the problem depends on several parameters with wide ranges, the rest of possibilities can also be preferred. The transition to non-axisymmetric equatorially antisymmetric longitudinal waves, as was assumed in [17], was found in [35] for spherical shells with $\eta = 0.4$, Pr $= 0.01$, Ek $< 10^{-5}$, and m between 14 and 16. The so-called torsional periodic modes of convection, axisymmetric ($m = 0$) and equatorially antisymmetric, were found numerically in the case of rotating fluid spheres for Pr $\ll 0.01$ at low Ek when $\mathrm{Pr}/\mathrm{Ek} = \mathcal{O}(10)$, and with isothermal and stress-free boundary conditions [36]. Their existence was confirmed by using asymptotic methods [37]. It was also proved there that the torsional modes are never preferred with non-slip boundary conditions. After these results, the nonlinear dynamics of these flows was studied [38] for $\mathrm{Pr} = 0.01$, $\mathrm{Ek} = 10^{-3}$, by means of time integration in a spherical shell of very small radius ratio $\eta = 0.001$, finding a latitudinal propagation of the patterns of convection, and the loss of stability of the axisymmetric solutions very close to their onset. The non-linear torsional solutions and the bifurcated quasiperiodic and chaotic regimes were also found when the axisymmetry is enforced [39]. Very recently a detailed study of the three-dimensional flows also in a spherical shell with $\eta = 0.01$, and for $\mathrm{Pr} = 10^{-3}$ and $\mathrm{Ek} = 10^{-4}$ was performed in [40] for a large range of Rayleigh numbers. Mixed dynamics in which nonlinear superpositions of the torsional solutions and azimuthal waves were observed. This leads to meandering motions of the spots of kinetic energy near the surface of the sphere. Different sequences of stable states of convection with different symmetries were identified and described from the onset of the oscillations to the temporally chaotic dynamics. It was seen that a remnant of it is present even at large Ra up to temporal chaos. It was also found, just by simulations, that the Neimark-Sacker bifurcation from the periodic torsional solutions leads to an azimuthal wave number $m = 2$. This happens very close to the onset of convection after very long transients, and therefore the exact value of the critical Ra was difficult to obtain. Moreover, since those computations were for a spherical shell with a very small core, it was not clear that the same instability was to be found in the case of the full sphere. In addition it was difficult to understand the sequence of bifurcations found there due to the proximity to each other.

The aim of this article is to study the transitions to azimuthal dependence from the axisymmetric solutions of convection in a rotating fluid sphere, uniformly heated from the interior, and with isothermal and stress-free boundary conditions. Several pairs of parameters $(\mathrm{Pr}, \mathrm{Ek})$ are selected covering the full region, computed in [41], in which the torsional solutions are the preferred flows after the outset of convection from the conduction state. It includes from liquid metals to gases. In contrast to previous studies, the periodic solutions are calculated by using a continuation method, and their stability is analyzed. Consequently, the critical points where the quasiperiodic solutions arise are determined with a precision that it is impossible to achieve just with numerical simulations. The critical Ra, wave number, and new frequencies at the secondary bifurcation are computed, and some features of the eigenfunctions are described. As seen in this article, the transitions separate when Ek is greater than that used in [40], and it is expected that this will help to have a better view of the possible sequences of solutions leading to complex flows.

The rest of the paper is organized as follows. The formulation of the problem is established in Section II, and the numerical methods used are briefly described in Section III. Section IV summarizes some previous results on the determination of the region where the torsional solutions are preferred, and Section V presents the main results on their continuation and stability to azimuthal dependence. Finally, Section VI includes some conclusions and remarks.

II. FORMULATION OF THE PROBLEM

The thermal convection of a rotating and uniformly internally heated fluid sphere is considered. A radial gravity $\mathbf{g} = -\gamma \boldsymbol{r}$, with $\gamma > 0$, is assumed corresponding to a uniform density. The surface is supposed to be at a constant temperature T_o. The Boussinesq approximation of the mass, momentum and energy equations is written in the rotating frame of reference of the sphere. The centrifugal force is neglected since $\Omega^2/\gamma \ll 1$ in the major planets and stars, $\boldsymbol{\Omega} = \Omega \hat{e}_z$ being the constant angular velocity. Moreover, the density is also considered as constant in the Coriolis term.

To write the equations in non-dimensional form the following scales are considered: the radius of the sphere, r_o, for the distance, a viscous time, r_o^2/ν, and $\nu^2/\gamma\alpha r_o^4$ for the temperature. The physical constants in these expressions are the kinematic viscosity, ν, and the thermal expansion coefficient α.

In the Boussinesq approximation the dependence of the density of the fluid with the temperature is only considered in the buoyancy term, and then the divergence-free velocity field can be written in terms of toroidal and poloidal scalar potentials [16], i.e.,

$$\boldsymbol{v} = \boldsymbol{\nabla} \times (\Psi \boldsymbol{r}) + \boldsymbol{\nabla} \times \boldsymbol{\nabla} \times (\Phi \boldsymbol{r}).$$

The equations for Ψ and Φ are the radial components of the curl and double curl of the Navier-Stokes equations. That for the temperature is written for the perturbation of the conduction state $\boldsymbol{v} = \mathbf{0}$ and $\mathrm{T}_c(r) = \mathrm{T}_o + (q/6\kappa c_p)(r_o^2 - r^2)$, q being the rate of internal heat generation per unit mass, c_p the specific heat at constant pressure, and κ the thermal diffusivity. With the present formulation the conduction state is always a solution for any value of the parameters, although unstable for large enough Ra. The final equations are then

$$(\partial_t - \Delta)\,\mathcal{L}_2\Psi = 2\mathrm{Ek}^{-1}\,(\partial_\varphi\Psi - \mathcal{Q}\Phi) - \boldsymbol{r}\cdot\boldsymbol{\nabla}\times(\boldsymbol{\omega}\times\boldsymbol{v}), \tag{1}$$

$$(\partial_t - \Delta)\,\mathcal{L}_2\Delta\Phi = 2\mathrm{Ek}^{-1}\,(\partial_\varphi\Delta\Phi + \mathcal{Q}\Psi) - \mathcal{L}_2\Theta + \boldsymbol{r}\cdot\boldsymbol{\nabla}\times\boldsymbol{\nabla}\times(\boldsymbol{\omega}\times\boldsymbol{v}), \tag{2}$$

$$(\mathrm{Pr}\partial_t - \Delta)\,\Theta = \mathrm{Ra}\mathcal{L}_2\Phi - \mathrm{Pr}(\boldsymbol{v}\cdot\boldsymbol{\nabla}\Theta), \tag{3}$$

where $\boldsymbol{r}$ is the position vector, $\boldsymbol{\omega} = \boldsymbol{\nabla}\times\boldsymbol{v}$ is the vorticity, $\Theta(r,\theta,\varphi) = \mathrm{T}(r,\theta,\varphi) - \mathrm{T}_c(r)$ is the temperature deviation from the conduction state and (r,θ,φ) are the spherical coordinates, θ measuring the colatitude and φ the longitude. The operators $\mathcal{L}_2$ and $\mathcal{Q}$ are defined as $\mathcal{L}_2 = -r^2\Delta + \partial_r(r^2\partial_r)$ and $\mathcal{Q} = r\cos\theta\Delta - (\mathcal{L}_2 + r\partial_r)(\cos\theta\partial_r - r^{-1}\sin\theta\partial_\theta)$.

The non-dimensional parameters are the Rayleigh, Prandtl and Ekman numbers, defined as

$$\mathrm{Ra} = \frac{q\gamma\alpha r_o^6}{3c_p\kappa^2\nu}, \qquad \mathrm{Pr} = \frac{\nu}{\kappa}, \quad \text{and} \qquad \mathrm{Ek} = \frac{\nu}{\Omega r_o^2}, \tag{4}$$

respectively.

Impenetrable, stress-free, and constant temperature boundary conditions are considered, i.e., $\Phi = \partial^2_{rr}\Phi = \partial_r(\Psi/r) = 0$, $\Theta = 0$ at $r = r_o$. At $r = 0$ just regularity conditions are required.

The system (1)-(3) with the above boundary conditions is invariant under the group $SO(2)\times Z_2$ generated by the rotations about the axis of the sphere, $\mathcal{R}_{\varphi_0}$, and the equatorial reflection, $\mathcal{R}_{eq}$, defined by

$$\mathcal{R}_{\varphi_0}(v_r, v_\theta, v_\varphi)(t,r,\theta,\varphi) = (v_r, v_\theta, v_\varphi)(t,r,\theta,\varphi-\varphi_0),$$
$$\mathcal{R}_{\varphi_0}\Theta(t,r,\theta,\varphi) = \Theta(t,r,\theta,\varphi-\varphi_0),$$
$$\mathcal{R}_{eq}(v_r, v_\theta, v_\varphi)(t,r,\theta,\varphi) = (v_r, -v_\theta, v_\varphi)(t,r,\pi-\theta,\varphi),$$
$$\mathcal{R}_{eq}\Theta(t,r,\theta,\varphi) = \Theta(t,r,\pi-\theta,\varphi),$$

if $\boldsymbol{v} = (v_r, v_\theta, v_\varphi)$ in spherical coordinates.

III. NUMERICAL METHODS

To obtain the numerical solutions, Φ, Ψ and Θ are expanded in a triangular truncated spherical harmonic series up to a maximum degree and order L as

$$X(r,\theta,t)=\sum_{l=0}^{L}\sum_{m=-l}^{l}X_l^m(r,t)Y_l^m(\theta,\varphi),$$

where X represents any of them, Y_l^m being the spherical harmonics, normalized as

$$Y_l^m(\theta,\varphi)=\sqrt{\frac{2l+1}{2}\frac{(l-m)!}{(l+m)!}}P_l^m(\cos\theta)e^{im\varphi}=\tilde{P}_l^m(\cos\theta)e^{im\varphi},$$

for $l\geq 0$ and $-l\leq m\leq l$, $P_l^m(\cos\theta)$ being the associated Legendre functions of degree l and order m. The potentials are determined up to the addition of a radial function. This is solved by taking $\Phi_0^0=\Psi_0^0=0$. In order to find axisymmetric solutions, all the derivatives ∂_φ are taken as zero in all the equations, and the expansions are reduced to

$$X(r,\theta,t)=\sum_{l=0}^{L}X_l^0(r,t)\tilde{P}_l^0(\cos\theta).$$

The equations for the amplitudes of the expansions in the general case, required to compute the stability of the axisymmetric flows, are

$$\partial_t\Psi_l^m=\mathcal{D}_l\Psi_l^m+\frac{1}{l(l+1)}\Big[\frac{2}{\mathrm{Ek}}\left(im\Psi_l^m-[Q\Phi]_l^m\right)-[\mathbf{r}\cdot\nabla\times(\boldsymbol{\omega}\times\boldsymbol{v})]_l^m\Big],\tag{5}$$

$$\partial_t\mathcal{D}_l\Phi_l^m=\mathcal{D}_l^2\Phi_l^m-\Theta_l^m+\frac{1}{l(l+1)}\Big[\frac{2}{\mathrm{Ek}}\left(im\mathcal{D}_l\Phi_l^m+[Q\Psi]_l^m\right)+[\mathbf{r}\cdot\nabla\times\nabla\times(\boldsymbol{\omega}\times\boldsymbol{v})]_l^m\Big],\tag{6}$$

$$\partial_t\Theta_l^m=\mathrm{Pr}^{-1}\mathcal{D}_l\Theta_l^m+\mathrm{Pr}^{-1}l(l+1)\mathrm{Ra}\Phi_l^m-[\boldsymbol{v}\cdot\nabla\Theta]_l^m,\tag{7}$$

for $0\leq l\leq L$ and $-l\leq m\leq l$, and where $\mathcal{D}_l=\partial_{rr}^2+(2/r)\partial_r-(l(l+1)/r^2)$, and the symbol $[f]_l^m$ means the coefficient multiplying Y_l^m in the spherical harmonic expansion of an arbitrary function f. The coupling between different degrees, l, is through the nonlinear terms and the linear operator Q since

$$[Qf]_l^m=-l(l+2)c_{l+1}^mD_{l+2}^+f_{l+1}^m-(l-1)(l+1)c_l^mD_{1-l}^+f_{l-1}^m,$$

with $D_l^+f=\partial_rf+lf/r$, and $c_l^m=[(l^2-m^2)/(4l^2-1)]^{1/2}$. In the case of the order, m, it is only due to the quadratic terms (the rightmost in every equation).

The linearization of Eqs. (5)-(7) about an axisymmetric solution giving rise to a velocity field $\boldsymbol{v}_a$, a vorticity $\boldsymbol{\omega}_a = \nabla \times \boldsymbol{v}_a$, and a deviation of the temperature Θ_a consists only in replacing the three quadratic terms by

$$[\mathbf{r} \cdot \nabla \times (\boldsymbol{\omega}_a \times \boldsymbol{v} + \boldsymbol{\omega} \times \boldsymbol{v}_a)]_l^m, \tag{8}$$

$$[\mathbf{r} \cdot \nabla \times \nabla \times (\boldsymbol{\omega}_a \times \boldsymbol{v} + \boldsymbol{\omega} \times \boldsymbol{v}_a)]_l^m, \tag{9}$$

$$[\boldsymbol{v}_a \cdot \nabla\Theta + \boldsymbol{v} \cdot \nabla\Theta_a]_l^m, \tag{10}$$

respectively. Then the equations for different orders m are no longer coupled. In this way the study of the linear stability of an axisymmetric solution separates into a collection of problems, one for each azimuthal wave number m. This is always the case in systems having an $O(2)$ or $SO(2)$ group of symmetries in one of the coordinates, with an initial solution invariant under the group.

The system of PDEs (5)-(7) is finally discretized in the radial direction to obtain a systems ordinary differential equations (ODEs). A collocation method on a Gauss-Lobatto mesh of $N+1$ points is used. The regularity conditions imply (see for instance [42]) that $X_l^m(r,t) = r^l Z_l^m(r,t)$, with $Z_l^m(r,t)$ even in r and smooth. Therefore, if $l > 0$, X_l^m and its radial derivatives up to order $l-1$ must vanish at $r=0$, but we only enforce $X_l^m(r=0)=0$ if $l>0$ in the discretized radial differential operators, which include the boundary conditions at $r=r_0$. If $l=0$ the only additional condition is $\partial_r X_0^0(r=0)=0$. This is only needed for the temperature since $\Phi_l^0 = \Psi_l^0 = 0$. It was shown in [43] that imposing only these conditions is enough to obtain consistent results for the linear stability analysis of the conduction state, avoiding several types of spurious modes. It can be checked *a posteriori* that the amplitudes satisfy accurately all the regularity conditions.

The system (5)-(7) for the axisymmetric solutions, i.e. only for the $m=0$ amplitudes, and discretized also in r, will be written as

$$\dot{\boldsymbol{u}}_0 = \mathcal{L}_0 \boldsymbol{u}_0 + \mathcal{N}(\boldsymbol{u}_0, \boldsymbol{u}_0). \tag{11}$$

It is a set of real ODEs of dimension $(3L+1)(N-1)$. The vector $\boldsymbol{u}_0$ contains the value of the amplitudes at the internal collocation nodes. The linearized equations about $\boldsymbol{u}_0$ for a single azimuthal wave number m will be written as

$$\dot{\boldsymbol{u}}_m = \mathcal{L}_m \boldsymbol{u}_m + \mathcal{N}(\boldsymbol{u}_0, \boldsymbol{u}_m) + \mathcal{N}(\boldsymbol{u}_m, \boldsymbol{u}_0). \tag{12}$$

It is a set of complex ODEs of dimension $3(L-m+1)(N-1)$. The vector $\boldsymbol{u}_m$ contains the amplitudes of order m of the spherical harmonic expansion at the internal collocation nodes.

The linear parts $\mathcal{L}_m$ depend on the three nondimensional parameters (4), and have a block-tridiagonal shape due to the operator $\mathcal{Q}$. The symbol $\mathcal{N}$ represents the quadratic operators coming from the advection terms in the equations. Due to the diffusion these systems of ODES are *stiff*, so they are integrated by means of the fully implicit LSODPK solver of the ODEPACK package [44] or by our own fifth-order semi-implicit method (IMEX), based on backward-differentiation-extrapolation formulas described, for instance in [45]. Since stress-free boundary conditions are applied, the three components of the angular momentum per unit mass, relative to an inertial frame of reference,

$$\mathbf{L}(t) = \int_V \boldsymbol{r} \times \boldsymbol{v}(t, \boldsymbol{r}) d\boldsymbol{r},$$

V being to the volume occupied by the fluid, are constants of the movement, and the numerical methods must conserve them. This is done by adding a small body force correcting the possible deviations, as explained in the Appendix of [39]. This affects only the equations for Ψ_1^0 when $m=0$, and the real and imaginary parts of Ψ_1^1 when $m=1$ (see, for instance, [46]). There are other ways to proceed, as for instance, modifying the boundary conditions for these three radial functions.

The method to compute the periodic solutions of the system (11) was explained in [39]. Matrix-free continuation techniques are applied to the set of equations

$$\boldsymbol{u}_0 - \boldsymbol{\phi}_0(T, \boldsymbol{u}_0, p) = 0 \tag{13}$$

$$g(\boldsymbol{u}_0, p) = 0 \tag{14}$$

for $(T, \boldsymbol{u}_0, p)$, where T is the period, p is a parameter of the problem that for the present calculations will be $p = \mathrm{Ra}$ (the other two will be kept fixed to several pairs of values), $\boldsymbol{\phi}_0(t, \boldsymbol{u}, p)$ is the solution of (11) with $\boldsymbol{\phi}_0(0, \boldsymbol{u}_0, p) = \boldsymbol{u}_0$, and $g(\boldsymbol{u}_0, p) = 0$ is a phase condition to select just one point on each periodic orbit. It can be, for instance, the Poincaré condition $g(\boldsymbol{u}_0, p) = \dot{\boldsymbol{u}}_{0,prev} \cdot (\boldsymbol{u} - \boldsymbol{u}_{0,prev}) = 0$, where $\boldsymbol{u}_{0,prev}$ is the point obtained on the previous computed periodic orbit, and $\dot{\boldsymbol{u}}_{0,prev}$ its tangent. The torsional solutions, $\boldsymbol{u}_0(t)$, are symmetric cycles, i.e., they satisfy $\boldsymbol{u}_0(T/2) = \mathcal{R}_{eq}\boldsymbol{u}_0(0)$. Therefore, this spatio-temporal symmetry can be used to halve the integration time in the calculation of $\boldsymbol{u}_0$.

The curves of torsional solutions were first found, as functions of Ra, for the pairs of values of $(\mathrm{Pr}, \mathrm{Ek})$ shown in Table I. The reason for choosing these values is explained later.

Pr	Ek	Pr/Ek	Pr	Ek	Pr/Ek
1.e-3	1.e-4	10.00	0.4	2.9498e-2	13.56
1.e-2	1.e-3	10.00	0.5	3.5304e-2	14.16
5.e-2	5.e-3	10.00	0.6	4.0796e-2	14.70
0.1	9.275e-3	10.78	0.7	4.6000e-2	15.21
0.2	1.6705e-2	11.97	0.8	5.1026e-2	18.62
0.3	2.3328e-2	12.86	0.9	5.5873e-2	16.10

TABLE I. Pairs of parameters $(\mathrm{Pr}, \mathrm{Ek})$ used in the calculations.

To study the stability, the branches of periodic orbits are post-processed. The Floquet multipliers corresponding to several wave numbers m are computed to detect either a Neimark-Sacker or other type of bifurcations. Since matrix-free Arnoldi or subspace methods are used, only the action of the monodromy matrix is required. This implies integrating the coupled systems (11), with initial condition $\boldsymbol{u}_0$, the solution of (13)–(14), and (12) with an arbitrary initial condition $\boldsymbol{u}_m(0)$. The leading (greater modulus) Floquet multipliers and the corresponding eigenfunctions are obtained. Details on these large-scale matrix-free methods for the cycles and their stability can be found in [47] or in the review on continuation methods for PDEs [48]. The same computations for the pairs $(\mathrm{Pr}, \mathrm{Ek}) = (10^{-2}, 10^{-3})$ and $(\mathrm{Pr}, \mathrm{Ek}) = (10^{-3}, 10^{-4})$ were first reported in [39], but only the secondary bifurcations to axisymmetric flows were studied. The subsequent quasiperiodic and chaotic flows, keeping the rotational invariance, were also described there.

The global data represented in the figures is the kinetic energy density, $k(t, r, \theta, \varphi) = (\boldsymbol{v} \cdot \boldsymbol{v})/2$, averaged over the whole volume of the sphere, V, and over the period of the periodic orbits. The volume average, $K(t)$, turns out to be

$$K(t) = \frac{1}{V} \int_V k(t, r, \theta, \varphi)\, dV = \frac{3\sqrt{2}}{2 r_o^3} \int_0^{r_o} r^2 k_0^0(r, t)\, dr,$$

where k_0^0 is the coefficient of order and degree 0 of the expansion of k in spherical harmonics. Its time average is

$$\overline{K} = \frac{1}{T} \int_0^T K(t)\, dt,$$

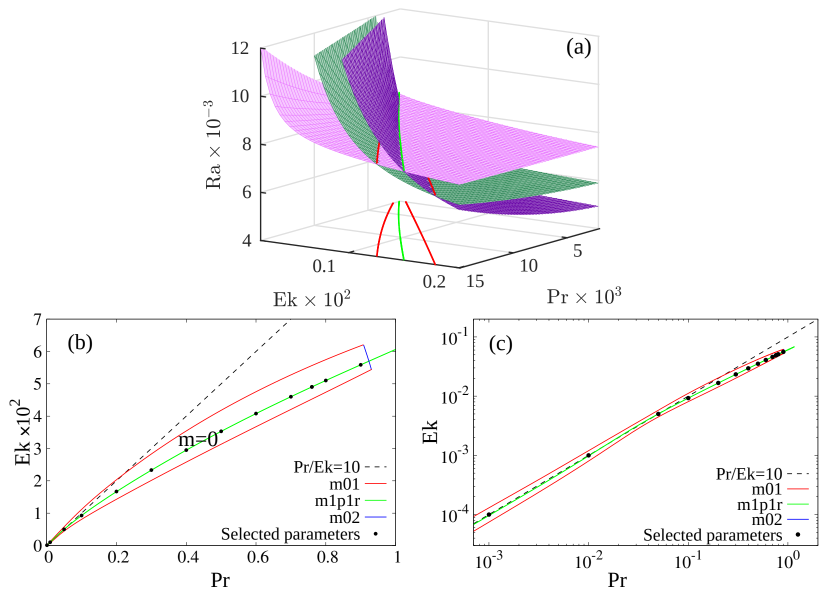

FIG. 1. (a) Surfaces of Hopf points corresponding to $m = 0$ (middle surface, in green), retrograde $m = 1$ waves (lower surface at the right, in dark violet) and prograde $m = 1$ waves (upper surface at the right, in light violet), close to $(\mathrm{Pr}, \mathrm{Ek}) = (0, 0)$ in the three-dimensional parameter space. The conduction state is stable below the three surfaces. Their intersections are small portions of the double Hopf curves m01p, m01r (in red) and m1p1r (in green). They have also been projected onto the plane $\mathrm{Ra} = 4 \times 10^3$. (b) Region inside which the first bifurcation is to axisymmetric solutions in linear scale, and (c) in logarithmic scale. The line $\mathrm{Pr}/\mathrm{Ek} = 10$ is represented with a dashed black line.

T being the period of the torsional solution. The time integral is approximated by the trapezoidal rule. From now $\overline{K}$ will be called mean energy, for simplicity.

The truncation parameters used for the present calculations are $(N, L) = (30, 50)$. It was checked in [39] that the relative error for several global quantities, including $\overline{K}$, was below 10^{-4} when the resolution was changed from $(N, L) = (30, 50)$ to $(N, L) = (40, 60)$, for values of Ra higher than those used here.

IV. SUMMARY OF PREVIOUS RESULTS.

Figure 1 summarizes the main results obtained in [41], which explain the selection of the parameters of Table I for the calculations of this study. Figure 1(a) shows the transition surfaces from the trivial conduction state to periodic axisymmetric solutions ($m = 0$, surface in green), and to azimuthal traveling waves with wave number $m = 1$ (two surfaces in violet). For the values in this plot one of the latter corresponds to retrograde waves traveling westwards (dark violet), and the other to prograde waves traveling eastwards (light violet). The conduction state is stable below the envelope of the surfaces, and becomes unstable when it is crossed, generically at a Hopf bifurcation.

The region in the Pr-Ek plane into which the first transition is to axisymmetric solutions, when Ra is increased, and Ek and Pr are kept fixed, is shown in Fig. 1(b), and will be described, for short, as the $m = 0$ region. It is bounded by the curves of double-Hopf points corresponding to simultaneous bifurcations from the conduction state to two different azimuthal wave numbers $(m = 0, m = 1)$ or $(m = 0, m = 2)$ (the surface for $m = 2$ is not represented in Fig. 1(a)). The limiting curves are the projections of intersections of the surfaces. They are shown in the plane $\mathrm{Ra} = 4 \times 10^3$ of Fig. 1(a), in Fig. 1(b), and in Fig. 1(c) in logarithmic scale. The latter shows that for any Pr near zero there is always a non-empty interval of Ek contained in the $m = 0$ region.

There are two double-Hopf curves for $(m = 0, m = 1)$ (in red in the figures and labeled as m01). Along the upper curve of Fig. 1(b) the transition to $m = 1$ gives rise to retrograde waves, while in the lower they are prograde if $\mathrm{Pr} < 0.7148$ and retrograde if $\mathrm{Pr} > 0.7148$. The system solved for the double-Hopf points (Eqs. (3.4)–(3.9) in [41]) gives the critical frequencies corresponding to the bifurcations to $m = 0$, which preserves the axisymmetry, and to $m = 1$, which breaks it. The sign of the second frequency determines if the corresponding azimuthal wave is prograde or retrograde. The upper and lower curves join at a turning point at $\mathrm{Pr} \approx 1.18$. This is not shown here because it happens out of the region of interest. The last bounding segment is part of the curve of double-Hopf bifurcations $(m = 0, m = 2)$ (in blue and labeled as m02) (see more details in [41]).

Along the intersection of the two $m = 1$ surfaces (in light green and labeled as m1p1r) two simultaneous Hopf bifurcations take place to waves traveling in opposite directions. This happens when the conduction state is already unstable to axisymmetric perturbations.

The projection of this curve onto the Pr-Ek plane is inside the $m = 0$ region and for this reason it has been used just as a reference to select the pairs of values of $(\mathrm{Pr}, \mathrm{Ek})$ used in the calculations. The black dots in Figs. 1(b) and 1(c) correspond to the values in Table I. Those of Pr were taken equally spaced from 0.1 to 0.9, and the cases $\mathrm{Pr} = 10^{-2}$ and $\mathrm{Pr} = 10^{-3}$, which were studied in the pure axisymmetric case in [41], were also included. The value $\mathrm{Pr} = 0.05$ was also considered in order to have another point close to the transition to very low Pr. The associated values of Ek have been taken to have points very close to the m1p1r curve.

The line $\mathrm{Pr}/\mathrm{Ek} = 10$ (dashed) has been added to Figs. 1(b) and 1(c). The computations in [36] and the theory in [37] predicted that along this line, and for low Pr, the first bifurcation of the conduction state leads to torsional solutions. It can be seen in Fig. 1(c) that this is the case below $\mathrm{Pr} \approx 0.22$.

V. CONTINUATION AND STABILITY OF THE PERIODIC ORBITS.

In order to compute the curves of periodic orbits parameterized by Ra, for the pairs of values of $(\mathrm{Pr}, \mathrm{Ek})$ in Table I, it is necessary to find approximate initial conditions satisfying Eqs. (13)-(14). The real part of the eigenvector associated to the Hopf bifurcation at the critical Ra for the onset of convection, multiplied by a suitable factor can be used as an initial condition for $\boldsymbol{u}_0$, and the period can be taken as $T = 2\pi/\omega$, ω being the imaginary part of the eigenvalue. Another possibility is evolving Eq. 11 above, but close to the critical Ra, to reach a stable periodic orbit, and track the curve for lower and higher Ra. Both methods have been used here, but mainly the second for its simplicity. Figure 2(a) shows the continuations of periodic torsional solutions for constant values of Pr and Ek in red, solid when they are stable, and dashed after the first bifurcation. The mean energy, $\overline{K}$, is represented versus Pr and Ra. It is scaled by Ek^{-2} to make all the curves approximately of the same height because K grows as Ek^{-2}.

The transverse curves in Fig. 2(a) correspond to the onset of the cycles and the bifurcations to azimuthal wave numbers $m = 0$, 1, 2 and 3. Only these are shown for two reasons. In previous works [38, 40] transitions to $m = 1$ and 2 were found for two pairs of small $(\mathrm{Pr}, \mathrm{Ek})$, so increasing values starting from $m = 0$ up to $m = 4$ have been studied. Moreover, when the transition to the latter takes place (always above that for $m = 3$ and beyond

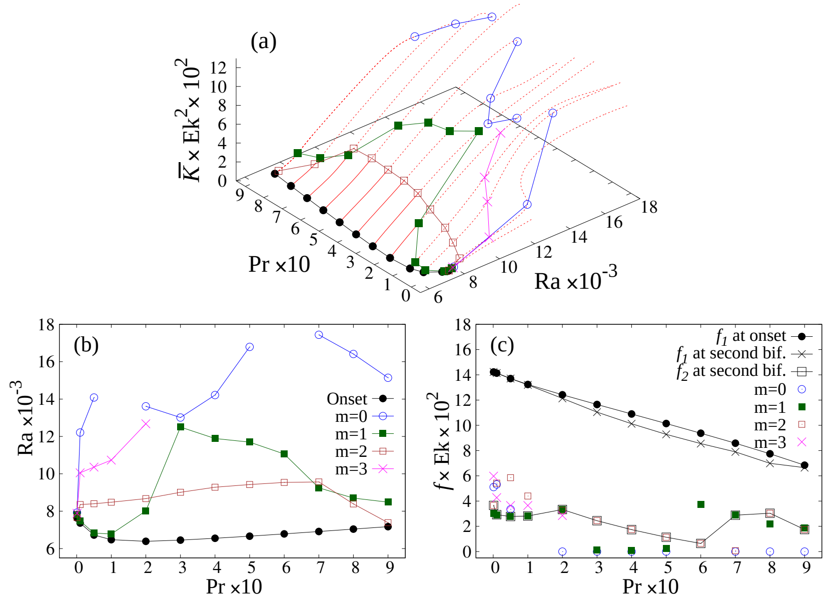

FIG. 2. (a) Curves of periodic orbits for the pairs of values of (Pr, Ek) of Table I (in red), solid/dashed when they are stable/unstable, and curves corresponding to the onset of the cycles (black, filled circles), and the bifurcations to $m = 0$ (blue, empty circles), $m = 1$ (green, filled squares), $m = 2$ (brown, empty squares) and $m = 3$ (magenta, crosses). (b) Projection of the bifurcation curves on the Pr-Ra plane. (c) Frequencies along the bifurcation curves of Fig. 2(b) using the same colors and symbols. The points of the curves for $m = 0$ to 3 are not joined by lines for clarity. The added black lines with crosses and empty squares are those of f_1 and f_2 at the transition to azimuthal dependence, respectively. Their values are shown in Table II.

Ra = 18000), the periodic orbits have, at least, six unstable Floquet multipliers. Therefore, it is difficult that higher wave numbers be relevant to this analysis.

It can be seen in Fig. 2(b) that the first bifurcation is to a wave number $m = 2$ for $\mathrm{Pr} \in [0.22, 0.69]$, approximately, and close to $\mathrm{Pr} = 10^{-3}$, and to $m = 1$ for $\mathrm{Pr} \in [10^{-2}, 0.22]$ and close to Pr = 0.7. The transition to $m = 2$ for $\mathrm{Pr} = 10^{-3}$ and $\mathrm{Ek} = 10^{-4}$, giving rise to quasiperiodic flows, was found previously by time integration in the case of a spherical shell of a radius ratio $\eta = 0.01$ (see second row of Fig.5 in [40]). The results obtained here

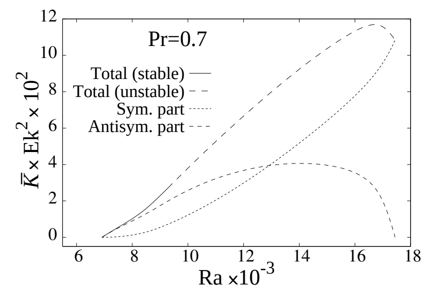

FIG. 3. Curve of periodic orbits for Pr = 0.7 showing the decomposition of the kinetic energy into its symmetric and antisymmetric parts relative to the equatorial reflection.

confirm that the quasiperiodic dynamics comes from this bifurcation, and that it is not related to having a small core. With the new information about the secondary critical Ra, it is now sure that this bifurcation is subcritical. When Pr goes to zero all the transitions to quasiperiodicity accumulate close to the first from the conduction state. For instance, for $\mathrm{Pr} = 10^{-3}$ the onset of convection occurs at Ra = 7637, and the bifurcations to $m = 2$, 1, 3, and 0 at Ra = 7658, 7818, 7886 and 7920, respectively. This explains the quick change of dynamics found in [40] when moving parameters, and why it is so difficult trying to understand what happens near the onset just by numerical simulations.

Table II displays some data relative to the bifurcations from the periodic torsional solutions. The columns contain the Pr and Ek numbers selected to do the computations (those of Table I), the critical Ra for the onset of the axisymmetric solutions, $\mathrm{Ra}_\mathrm{c}^{\mathrm{m}=0}$, that for the transition to azimuthal dependence, $\mathrm{Ra}_\mathrm{c}^{\mathrm{m}=\mathrm{m}_\mathrm{c}}$, which can be to $m = 1$ or $m = 2$ as seen in Fig. 2 and it is indicated in the fifth column, the first frequency $f_1 = 1/T$, T being the period of the periodic orbit $\boldsymbol{u}_0(t)$, and the second frequency appearing at the transitions to three-dimensional solutions, f_2.

The critical eigenfunctions $\boldsymbol{u}_m(t)$ are solution of (12) that satisfy $\boldsymbol{u}_m(T) = \exp(\pm i\rho)\boldsymbol{u}_m(0)$ for some phase ρ. At a Neimark-Sacker bifurcation the linear stability analysis gives Floquet multipliers $\exp(\pm i\rho)$, for some phase $\rho \in (0, \pi)$. From Floquet theory it is known that $\boldsymbol{u}_m(t) = \boldsymbol{u}_m^p(t)\exp(2\pi i f_2 t)$, with $\boldsymbol{u}_m^p(t)$ periodic of period T (and frequency f_1), and f_2 being the second frequency we are interested in (see [49]). At $t = T$ we have $\boldsymbol{u}_m(T) = \boldsymbol{u}_m^p(T)\exp(2\pi i f_2 T) = \boldsymbol{u}_m(0)\exp(2\pi i f_2 T)$. Therefore, ρ and $2\pi f_2 T$ might differ in a multiple

Pr	Ek	$\mathrm{Ra}_c^{m=0}$	$\mathrm{Ra}_c^{m=m_c}$	m_c	$f_1 = 1/T$	f_2
1.e-3	1.e-4	7637	7658	2	1423.	365.6
1.e-2	1.e-3	7366	7478	1	141.4	29.19
5.e-2	5.e-3	6722	6818	1	27.41	5.554
0.1	9.275e-3	6474	6772	1	14.24	3.039
0.2	1.6705e-2	6386	8037	1	7.263	1.994
0.3	2.3328e-2	6452	9010	2	4.735	1.049
0.4	2.9498e-2	6551	9263	2	3.433	0.5889
0.5	3.5304e-2	6663	9424	2	2.630	0.3219
0.6	4.0796e-2	6784	9536	2	2.097	0.1582
0.7	4.6000e-2	6911	9250	1	1.717	0.6270
0.8	5.1026e-2	7041	8388	2	1.370	0.5954
0.9	5.5873e-2	7172	7358	2	1.190	0.3123

TABLE II. Parameters Pr, Ek and critical Ra at the first two bifurcations, and frequencies at the secondary bifurcation for $m = 1$ or $m = 2$.

of 2π, i.e., $2\pi f_2 T = \rho + 2\pi n$, for some integer n. From this expression $f_2 = (\rho/2\pi + n) f_1$. In Table II n has been taken as zero, and the only difference in f_2 could be an integer multiple of f_1. The two frequencies and their integer linear combinations should be approximately found in the frequency analysis of the simulations close, but above, the parameters shown, except probably in the subcritical cases, which cannot be predicted just by looking at the stability. It has been checked that this is so for simulations with $\mathrm{Pr} = 0.01$, 0.1 and 0.715 in the case of a shell of $\eta = 0.001$ to confirm that everything matches.

Figure 2(c) shows all the frequencies along the transition curves of Fig. 2(b) scaled by Ek^{-1}. Those of the periodic torsional solutions, $f_1 = 1/T$, are presented in black curves, with full circles at the onset of the torsional solutions and with crosses at the transition to azimuthal dependence. The values on the latter are contained in column f_1 of Table II. The second frequency, f_2, appearing at this transition is shown with a black curve and empty square symbols (column f_2 of Table II). As explained before, its points correspond to points on the curves $m = 1$ or $m = 2$. The rest of symbols for $m = 0$ to 3 correspond to the frequency f_2, and have not been joined by lines for clarity. In the case of $m = 0$, $f_2 = 0$

for $\mathrm{Pr} \geq 0.2$ indicating that the transition is not a Neimark-Sacker bifurcation, but another Hopf from an axisymmetric steady state or a pitchfork bifurcation of periodic orbits (see comments below to the cases $\mathrm{Pr} = 0.7$, 0.8 and 0.9, and to Fig. 3).

It is seen that all frequencies go essentially as $f \sim \mathrm{Ek}^{-1}$, the product $f_1\mathrm{Ek}$ decreases slightly and monotonically with Pr, and its range of variation from the first to the second bifurcations is relatively small. This scaling was selected because the first instability is due to the Coriolis term. The variation with Pr of $f_2\mathrm{Ek}$ is more irregular. Two azimuthal wave numbers are involved. Moreover, it seems, by looking at Fig. 2(b), that the curves of transitions to $m = 1$ and 2 might be the envelopes of several curves. This also happens in the case of the bifurcation from the conduction state to azimuthal waves in the case of a shell [6]. This contributes to the more complicated behavior of f_2.

When the curves for $m = 0$ and 3 are reached, by increasing Ra, the torsional solutions are already unstable to perturbations to $m = 1$ and 2. Four Floquet multipliers are unstable. The wave numbers $m = 0, 3, 4$ are not preferred at the secondary transition and, in principle, solutions bifurcated form the torsional solutions with those azimuthal wave numbers would not be observed in simulations of the problem, because they would be unstable. They could be seen only if a time evolution approaches the unstable solutions. A trajectory might pass near several unstable objects (equilibria, periodic or quasiperiodic regimes) in a regular pattern. This has been observed before (see for instance Fig. 10 in [26]), and it is related to the existence of a heteroclinic chain, i.e., a closed sequence of trajectories joining the unstable objects. The computations presented in [40] reaching $\mathrm{Ra} = 14000$ do not show the presence of dominant azimuthal wave numbers other that $m = 1$ or 2.

The transition curves for $m = 0$ and $m = 3$ have gaps where the transition is above $\mathrm{Ra} = 18000$, which is the limit of the computations, or because the continuation curves do not reach this limit and the periodic flow is stable to perturbations of the given m in all its interval of existence. For instance this is what happens for $\mathrm{Pr} = 0.7$, 0.8, and 0.9 as can be seen in Fig. 2. In these cases the bifurcation to $m = 0$ above $\mathrm{Ra} = 14000$ is a Hopf point from an unstable steady state, which is non-trivial and invariant under equatorial reflections (the curves of these equilibria are not shown here). Fig. 3 shows the decomposition of the kinetic energy into its symmetric and antisymmetric parts relative to the equatorial reflection for $\mathrm{Pr} = 0.7$. It is one of the curves of fixed Pr in Fig. 2(a). The two endpoints at $\mathrm{Ra} = 6912$ and $\mathrm{Ra} = 17441$ correspond to Hopf bifurcations, the left one from the conduction state, and the right one from an unstable branch of equilibria. It has not been computed, but the periodic orbit at Ra = 17441 has a very small amplitude, which is not visible in a movie of the solution, and can be used to visualize the nearby equilibrium. As can be seen in Fig. 3, the antisymmetric part goes to zero at this point. Fig. 4 shows, Θ, k, and T for this steady solution. The flow can be seen as the superposition of two counter-rotating toroidal vortex, one in each hemisphere with the inflow at the equator, and an azimuthal velocity field, which depends on the radius and colatitude. It resembles two of the artificial velocity fields used by Dudley and James [50] to study the generation of magnetic fields by dynamo effect. The main difference is that the azimuthal component is more complex in our case. It must be stressed that these steady solutions are unstable to azimuthal perturbations, as the periodic orbits from which they bifurcate.

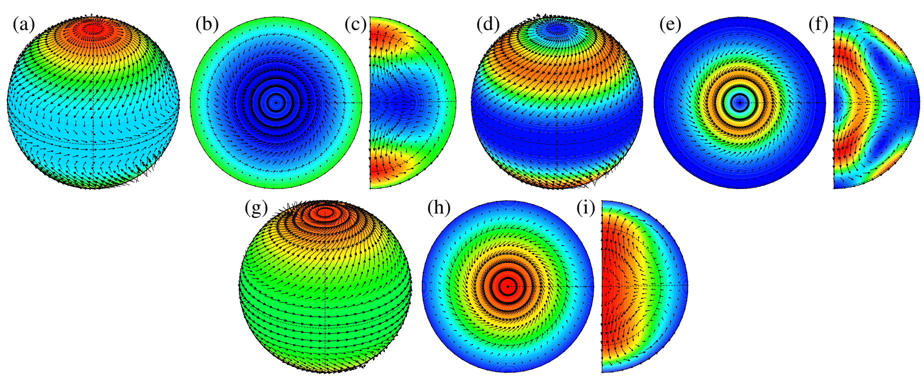

FIG. 4. Contour plots of (a)-(c) Θ, (d)-(f) k, and (g)-(i) T. The velocity field projected on each section is superposed in all plots. It is different over the spherical surfaces because the sections are different. The dashed lines in each section indicate the position of the other two. In the case of the energy the spherical section is very close to the outer surface. The parameters are Ra = 17440, Pr = 0.7, and Ek = 0.046, very close to an unstable equilibrium.

Figure 5 (Multimedia view) shows several snapshots of the time evolution of a torsional solution at the beginning of the branch of Pr = 0.7 in Fig. 3 at Ra = 6912. Since the

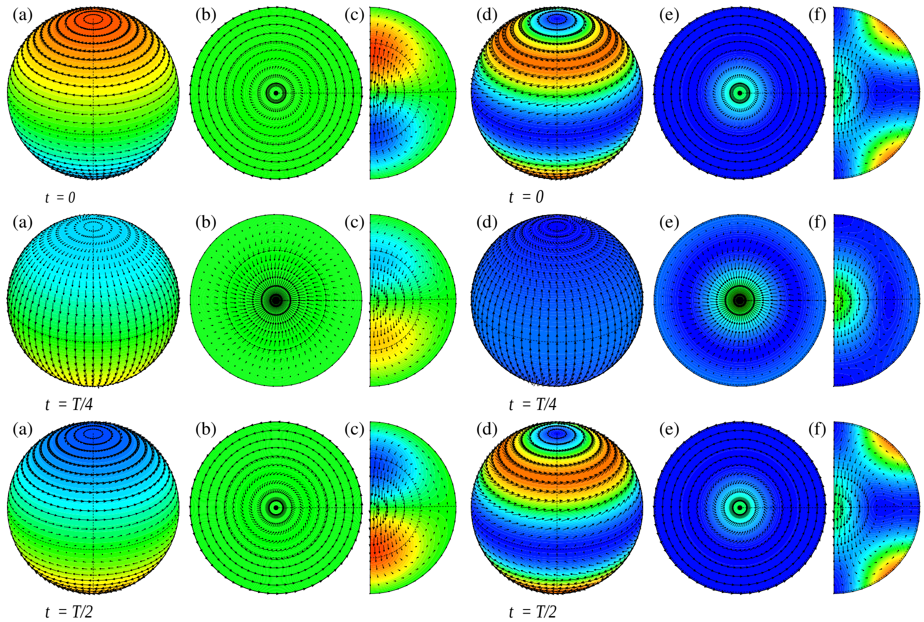

FIG. 5. Idem Fig. 4 only for (a)-(c) Θ and (d)-(f) k, for the fractions of the period, $T = 0.535909$, indicated. The parameters are $\mathrm{Ra} = 6912$, $\mathrm{Pr} = 0.7$, and $\mathrm{Ek} = 0.046$. (Multimedia view).

torsional periodic solutions are symmetric cycles, i.e.,

$$v_r(t + T/2, r, \theta, \varphi) = v_r(t, r, \pi - \theta, \varphi),$$
$$v_\theta(t + T/2, r, \theta, \varphi) = -v_\theta(t, r, \pi - \theta, \varphi),$$
$$v_\varphi(t + T/2, r, \theta, \varphi) = v_\varphi(t, r, \pi - \theta, \varphi),$$
$$\Theta(t + T/2, r, \theta, \varphi) = \Theta(t, r, \pi - \theta, \varphi),$$

only half of the period is represented, the other half can be obtained by applying the above symmetries. Close to the onset, the symmetric part of the solution is very small (see Fig. 3), and it looks almost antisymmetric, as the eigenfunction at the bifurcation point. This is no longer the case when the symmetric part grows due to the quadratic terms of Navier-Stokes equations, as can be seen in Fig. 6 (Multimedia view) for $\mathrm{Ra} = 9286$. This is the point at which there is a Neimark-Sacker bifurcation leading to azimuthal dependence with longitudinal wave number $m = 1$. In both cases the perturbation of the temperature fills the

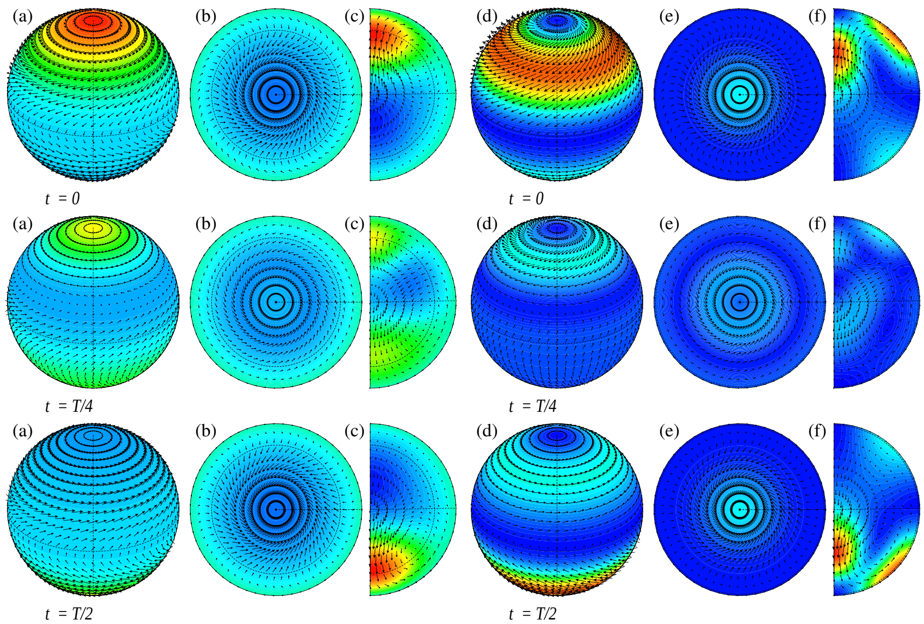

FIG. 6. Contour plots of (a)-(c) Θ and (d)-(f) k, and velocity field projected on each section, for the fractions of the period, $T = 0.582003$, indicated. The parameters are Ra $= 9286$, Pr $= 0.7$, and Ek $= 0.046$. (Multimedia view).

full domain. However, for Ra $= 6912$, k is concentrated at the surface when the longitudinal circulation reaches a maximum, or at the axis when the meridional circulation grows (see the vector fields). For Ra $= 9286$ both effects occur without a clear quarter-period time lag due to the growth of the symmetric part. Figure 7 shows the time evolution of k, and its decomposition into its symmetric and antisymmetric components relative to the equatorial symmetry, for both solutions. The symmetric part is very small for Ra $= 6912$, and therefore the antisymmetric part and the total k are almost the same. For Ra $= 9286$ both components are of the same order.

Figures 8 (Multimedia view) and 9 (Multimedia view) show, as representative of what is observed for the rest of large values of Pr, the contour plots and velocity fields corresponding to the critical eigenfunctions at the bifurcations to azimuthal wave number $m = 1$ at Ra $=$ 9286, and to $m = 2$ at Ra $= 9566$ along the branch of Pr $= 0.7$ (see Fig. 2(b)). The

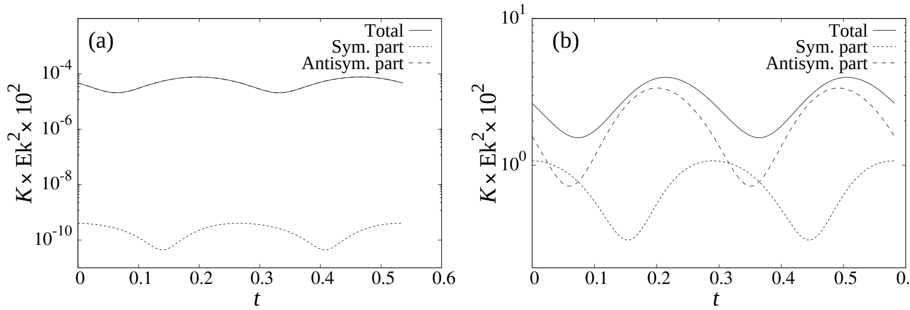

FIG. 7. Time evolution of $K(t)$, and its decomposition into the symmetric and antisymmetric parts for $\mathrm{Pr} = 0.7$, $\mathrm{Ek} = 0.046$. (a) $\mathrm{Ra} = 6912$ and (b) $\mathrm{Ra} = 9286$.

snapshots correspond to the fractions of the period of the base periodic orbit indicated. The transitions give rise to the appearance of a new frequency and hence to quasiperiodic regimes, which include an azimuthal drift and a latitudinal modulation of the torsional flows. At the bifurcation to azimuthal wave number $m = 1$ the frequencies mentioned previously are $(f_1, f_2) = (1.717, 0.6270)$, and at that to $m = 2$ they are $(f_1, f_2) = (0.1726, 0.01536)$.

The animation, close to the bifurcation to azimuthal wave number $m = 2$ for $\mathrm{Pr} = 10^{-3}$, showing the superposition $\boldsymbol{u}_0(t) + \varepsilon \boldsymbol{u}_m(t)$, with a suitable amplitude of the perturbation, ε, resembles the quasiperiodic solutions obtained in [40]. The position of the first bifurcation to the torsional solutions is almost the same, and was found to be supercritical in [39]. The second transition to azimuthal dependence is subcritical, since the modulated solutions were found for values below the Ra of the onset of the axisymmetric solutions [40]. Obtaining this information just by simulations is very difficult since, as said before, the transitions to different longitudinal wave numbers are very close together, and very long transients have to be computed to separate the different states.

There is a significant difference between the cases $\mathrm{Pr} = 0.7$ and $\mathrm{Pr} = 10^{-3}$. While in both cases the Neimark-Sacker bifurcation introduces an azimuthal drift with wave number $m = 2$, the latitudinal oscillation of the temperature perturbation of the eigenfunction $\boldsymbol{u}_m(t)$ is much larger for $\mathrm{Pr} = 0.7$. This makes the superposition for $\mathrm{Pr} = 10^{-3}$ to look very close to a linear combination of the torsional solution and a longitudinal wave. For $\mathrm{Pr} = 0.7$ the drift is masked by the latitudinal oscillations, giving rise to a direction reversing wave in the

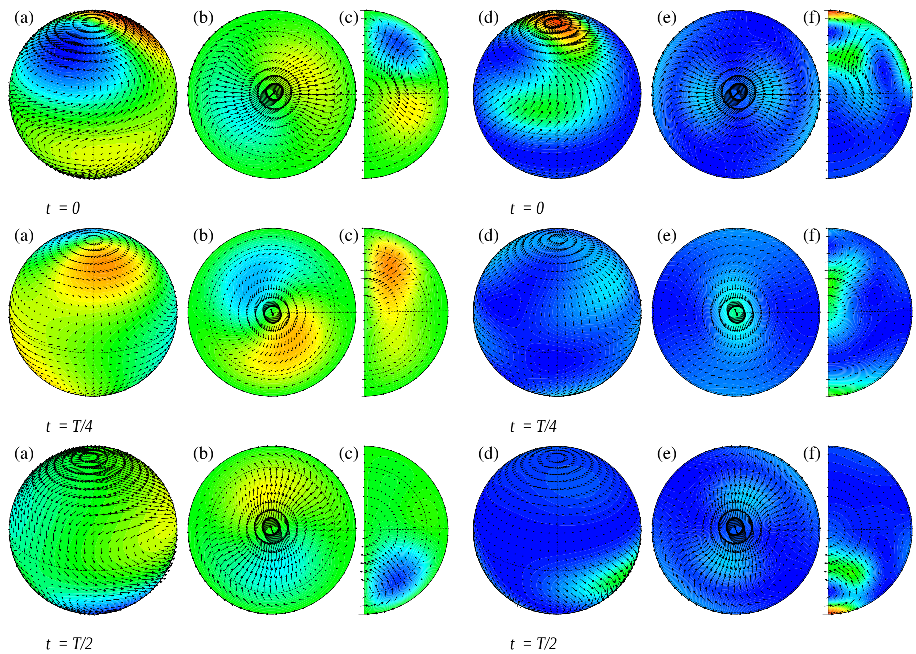

FIG. 8. Contour plots of (a)-(c) Θ and (d)-(f) k, and velocity field, for the eigenfunction of azimuthal wave number $m = 1$ at the Neimark-Sacker bifurcation, at the same times as its base periodic orbit shown in Fig. 6. In this case the eigenfunction is no longer periodic. The parameters are Ra = 9286, Pr = 0.7, and Ek = 0.046. The top row in each animation corresponds to the periodic orbit plus a multiple of the eigenfunction to see the effect of the bifurcation. The superposition is quasiperiodic and therefore it does not close after the two periods of the periodic orbit shown. The second row is a movie just of the eigenfunction. (Multimedia view).

equator. Then the global drift is better seen in the spherical projections.

VI. CONCLUSIONS AND CLOSING REMARKS

The stability of the axisymmetric periodic solutions of thermal convection in rotating fluid spheres has been studied, in the range of parameters for which they are the preferred pattern at the onset. The Neimark-Sacker bifurcations give rise to quasiperiodic flows of azimuthal

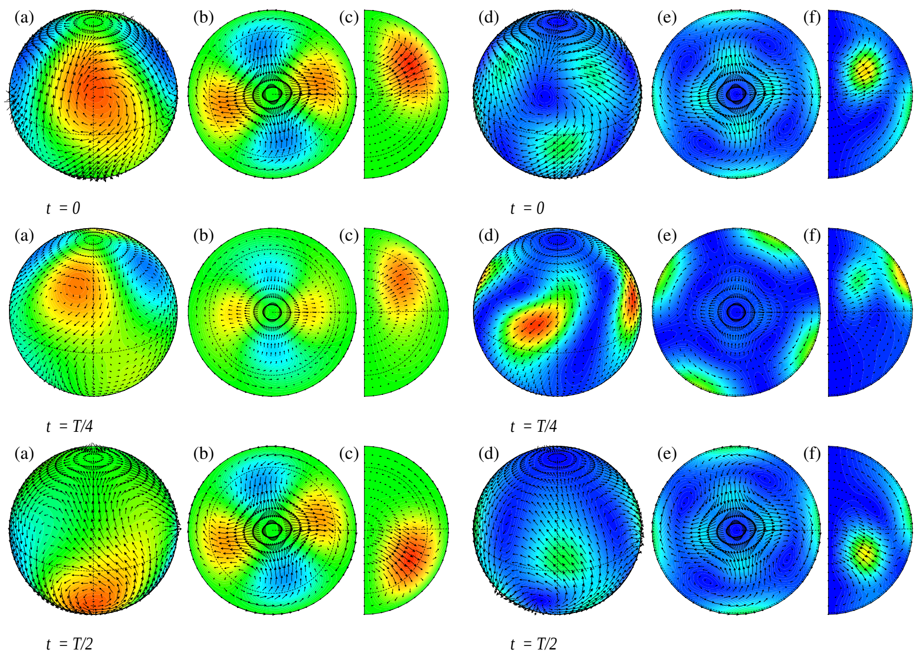

FIG. 9. Contour plots of (a)-(c) Θ and (d)-(f) k, and velocity field, for the eigenfunction of $m = 2$ at $\mathrm{Ra} = 9566$, at the fractions of the period of the periodic orbit, $T = 0.579350$, indicated. See the description of what is shown in the movies in the caption of Fig. 8 (Multimedia view).

wave numbers $m = 1$ or $m = 2$. They introduce a longitudinal drift, and a latitudinal modulation, which is very small for low Pr. The transitions to higher wave numbers appear only at much larger Ra except for very low Pr and Ek numbers. In this case the bifurcations accumulate close to the onset of convection, and consequently a complex spatio-temporal dynamics should be expected at low Ra.

The results agree with previous studies obtained by direct numerical simulations, and confirm that the quasiperiodic orbits of azimuthal wave number $m = 2$ found in [40] come from the Neimark-Sacker bifurcation of the torsional solutions. On the other hand, the astrophysical problems for which this research could be relevant, concern the latitudinal migrations of large-scale spots in the surface of celestial bodies as, for instance, in the Sun. The symmetry breaking transitions from axisymmetric periodic orbits to quasiperiodic flows for Pr < 0.93 supply mechanisms for the transport of large-scale spots of energy in latitude and longitude, and for the interchange of energy between the center and the surface of the sphere.

Dynamical systems tools, based on Newton-Krylov methods to find the periodic solutions, and Arnoldi or subspace methods to find the leading Floquet multipliers, have been used. They allow a more efficient study than using only numerical simulations, especially for periodic flows and close to the bifurcations where the transients are very long. However, the two ways complement each other. Although it is possible to track curves of generic quasiperiodic flows [30, 51], it is quite expensive for three-dimensional problems, and not much justified when the interval of the parameter in which this is useful is very small because there are nearby transitions to chaotic regimes. More efficient particular techniques can be used when the quasiperiodic regimes are modulated waves. Their computation can be reduced to that of periodic orbits in a frame of reference in which the original waves become steady flows. The prediction of the transitions from waves to modulated waves was developed in [52], and the reduction to cycles was applied, for instance, in [53] for the plane Poiseuille flow, and in [29] in the thermal convection in rotating spherical shells. For the present problem the quasiperiodic regimes are not bifurcated from rotating waves, and the perturbations are not just longitudinal waves, they include also latitudinal modulations. Then that techniques cannot be applied. The solutions will be always seen as quasiperiodic in any rotating frame of reference. This has been checked to be the case for spherical shells with a small inner radius in some regimes with low Pr.

There are many other fluid mechanics or reaction-diffusion problems for which the tools used here can be applied. In particular, when a periodic spatial direction is present, the separation of the stability problem of the periodic solutions, invariant along this direction, into the different wave numbers is an important simplification.

CONFLICT OF INTEREST

The authors have no conflicts to disclose.

DATA AVAILABILITY STATEMENT

The data that support the findings of this study are available from the corresponding author upon reasonable request.

ACKNOWLEDGMENTS

This research has been supported by the Spanish MCINN/FEDER PID2021-125535NB-I00 project.

[1] K. Zhang, X. Liao, and P. Earnshaw, "On inertial waves and oscillations in a rapidly rotating fluid spheroid," J. Fluid Mech. **504**, 1–40 (2004).

[2] B. M. Boubnov and G. S. Golitsyn, *Convection in Rotating Fluids*, Fluid Mechanics and its Applications, Vol. 29 (Kluwer Academic Publishers, 1995).

[3] Paul H Roberts and Eric M King, "On the genesis of the Earth's magnetism," Reports on Progress in Physics **76**, 096801 (2013).

[4] F. H. Busse, "Thermal instabilities in rapidly rotating systems," J. Fluid Mech. **44**, 441–460 (1970).

[5] E. Dormy, A. M. Soward, C. A. Jones, D. Jault, and P. Cardin, "The onset of thermal convection in rotating spherical shells," J. Fluid Mech. **501**, 43–70 (2004).

[6] M. Net, F. Garcia, and J. Sánchez, "On the onset of low-Prandtl-number convection in rotating spherical shells: non-slip boundary conditions," J. Fluid Mech. **601**, 317–337 (2008).

[7] F. Garcia, J Sánchez, and M. Net, "Numerical simulations of high-Rayleigh-number convection in rotating spherical shells under laboratory conditions," Phys. Earth Planet. Inter. **230**, 28–44 (2014).

[8] R. Monville, J. Vidal, D. Cébron, and N. Schaeffer, "Rotating double-diffusive convection in stably stratified planetary cores," Geophys. J. Int. **219**, S195–S218 (2019).

[9] C. Guervilly, P. Cardin, and N. Schaeffer, "Turbulent convective length scale in planetary cores," Nature **570**, 368–371 (2019).

[10] S. Liu, Z.-H. Wan, R. Yan, C. Sun, and D.-J. Sun, "Onset of fully compressible convection in a rapidly rotating spherical shell," J. Fluid Mech. **873**, 1090–1115 (2019).

[11] R. S. Long, J. E. Mound, C. J. Davies, and S. M. Tobias, "Scaling behaviour in spherical shell rotating convection with fixed-flux thermal boundary conditions," J. Fluid Mech. **889**, A7–1–32 (2020).

[12] T. T. Clarté, N. Schaeffer, S. Labrosse, and J. Vidal, "The effects of a robin boundary condition on thermal convection in a rotating spherical shell," Journal of Fluid Mechanics **918**, A36 (2021).

[13] Y. Lin and A. Jackson, "Large-scale vortices and zonal flows in spherical rotating convection," J. Fluid Mech. **912**, A46 (2021).

[14] C. J. Davies, D. Gubbins, and P. K. Jimack, "Scalability of pseudospectral methods for geodynamo simulations," Concurr Comput. **23**, 38–56 (2011).

[15] R. K. Yadav, T. Gastine, U. R. Christensen, S. J. Wolk, and K. Poppenhaeger, "Approaching a realistic force balance in geodynamo simulations," Proceedings of the National Academy of Sciences **113**, 12065–12070 (2016).

[16] S. Chandrasekhar, *Hydrodynamic and Hydromagnetic Stability* (Oxford University Press, New York, 1961).

[17] P. H. Roberts, "On the thermal instability of a rotating fluid sphere containing heat sources," Phil. Trans. R. Soc. Lond. A **263**, 93–117 (1968).

[18] A. M. Soward, "On the finite amplitude thermal instability in a rapidly rotating fluid sphere," Geophys. Astrophys. Fluid Dyn. **9**, 19–74 (1977).

[19] K. Zhang, "On coupling between the Poincaré equation and the heat equation," J. Fluid Mech. **268**, 211–229 (1994).

[20] C. A. Jones, A. M. Soward, and A. I. Mussa, "The onset of thermal convection in a rapidly rotating sphere," J. Fluid Mech. **405**, 157–179 (2000).

[21] K. Zhang and X. Liao, "A new asymptotic method for the analysis of convection in a rapidly rotating sphere," Journal of Fluid Mechanics **518**, 319–346 (2004).

[22] R. Meyer-Spasche and H. B. Keller, "Computation of the axisymmetric flow between rotating cylinders," J. Comput. Phys. **35**, 100–109 (1980).

[23] K. A. Cliffe, "Numerical calculations of the primary-flow exchange process in the Taylor problem," J. Fluid Mech. **197**, 57–79 (1988).

[24] C. K. Mamun and L. S. Tuckerman, "Asymmetry and Hopf bifurcation in spherical Couette flow," Phys. Fluids **7**, 80–91 (1995).

[25] J. Antonijoan, F. Marqués, and J. Sánchez, "Nonlinear spirals in the Taylor–Couette problem," Phys. Fluids **10**, 829–838 (1998).

[26] J. Sánchez, F. Garcia, and M. Net, "Computation of azimuthal waves and their stability in thermal convection in rotating spherical shells with application to the study of a double-Hopf bifurcation," Phys. Rev. E **87**, 033014 (2013).

[27] F. Feudel, N. Seehafer, L. S. Tuckerman, and M. Gellert, "Multistability in rotating spherical shell convection," Phys. Rev. E **87**, 023021 (2013).

[28] F. Feudel, L. S. Tuckerman, M. Gellert, and N. Seehafer, "Bifurcations of rotating waves in rotating spherical shell convection," Phys. Rev. E **92**, 053015 (2015).

[29] F. Garcia, M. Net, and J. Sánchez, "Continuation and stability of convective modulated rotating waves in spherical shells," Phys. Rev. E **93**, 013119 (2016).

[30] J. Sánchez, M. Net, and C. Simó, "Computation of invariant tori by Newton-Krylov methods in large-scale dissipative systems," Physica D **239**, 123–133 (2010).

[31] L. van Veen, G. Kawahara, and M. Atsushi, "On matrix-free computation of 2D unstable manifolds," SIAM J. Sci. Comput. **33**, 25–44 (2011).

[32] G. Kawahara, M. Uhlmann, and L. van Veen, "The Significance of Simple Invariant Solutions in Turbulent Flows," Ann. Rev. Fluid Mech. **44**, 203–225 (2012).

[33] H. A. Dijkstra, F. W. Wubs, A. K. Cliffe, E. Doedel, I. F. Dragomirescu, B. Eckhardt, A. Gelfgat, A. Hazel, V. Lucarini, A. Salinger, J. Sánchez, H. Schuttelaars, L. Tuckerman, and U. Thiele, "Numerical bifurcation methods and their application to fluid dynamics: Analysis beyond simulation," Commun. Comput. Phys. **15**, 1–45 (2014).

[34] M. Net and J. Sánchez, "Continuation of bifurcations of periodic orbits for large-scale systems," SIAM J. Appl. Dyn. Syst. **14**, 674–698 (2015).

[35] F. Garcia, J. Sánchez, and M. Net, "Antisymmetric polar modes of thermal convection in rotating spherical fluid shells at high Taylor numbers," Phys. Rev. Lett. **101**, 194501 (2008).

[36] J. Sánchez, F. Garcia, and M. Net, "Critical torsional modes of convection in rotating fluid spheres at high Taylor numbers," J. Fluid Mech. **791**, R1 (2016).

[37] K. Zhang, K. Lam, and D. Kong, "Asymptotic theory for torsional convection in rotating fluid spheres," J. Fluid Mech. **813**, R2–1–R2–11 (2017).

[38] D. Kong, K. Zhang, K. Lam, and A. P. Willis, "Axially symmetric and latitudinally propagating nonlinear patterns in rotating spherical convection," Phys. Rev. E **98**, 031101(R) (2018).

[39] J. Sánchez Umbría and M. Net, "Torsional solutions of convection in rotating fluid spheres," Phys. Rev. Fluids **4**, 013501 (2019).

[40] J. Sánchez Umbría and M. Net, "Three-dimensional quasiperiodic torsional flows in rotating spherical fluids at very low Prandtl numbers," Phys. Fluids **33**, 114103, pp14 (2021).

[41] J. Sánchez Umbría and M. Net, "Continuation of Double Hopf Points in Thermal Convection of Rotating Fluid Spheres," SIAM J. Appl. Dyn. Syst. **20**, 208–231 (2021).

[42] P. W. Livermore, C. A. Jones, and S. J. Worland, "Spectral radial basis functions for full sphere computations," J. Comput. Phys. **227**, 1209 – 1224 (2007).

[43] J. Sánchez, F. Garcia, and M. Net, "Radial collocation methods for the onset of convection in rotating spheres," J. Comput. Phys. **308**, 273 – 288 (2016).

[44] A. C. Hindmarsh, "ODEPACK, A Systematized Collection of ODE Solvers," in *Scientific Computing*, IMACS Transactions on Scientific Computation, Vol. 1, edited by R. S. Stepleman *et al.* (North-Holland, Amsterdam, 1983) pp. 55–64.

[45] F. Garcia, M. Net, B. García-Archilla, and J. Sánchez, "A comparison of high-order time integrators for the Boussinesq Navier-Stokes equations in rotating spherical shells," J. Comput. Phys. **229**, 7997–8010 (2010).

[46] C.A. Jones, P. Boronski, A.S. Brun, G.A. Glatzmaier, T. Gastine, M.S. Miesch, and J. Wicht, "Anelastic convection-driven dynamo benchmarks," Icarus **216**, 120–135 (2011).

[47] J. Sánchez, M. Net, B. García-Archilla, and C. Simó, "Newton-Krylov continuation of periodic orbits for Navier-Stokes flows," J. Comput. Phys. **201**, 13–33 (2004).

[48] J. Sánchez and M. Net, "Numerical continuation methods for large-scale dissipative dynamical systems," Eur. Phys. J. Special Topics **225**, 2465–2486 (2016).

[49] E. A. Coddington and N. Levinson, *Theory of ordinary differential equations* (McGraw-Hill, 1955).

[50] M. L. Dudley and R. W. James, "Time-dependent kinematic dynamos with stationary flows," Proc. Roy. Soc. Lond. A **425** (1989).

[51] J. Sánchez and M. Net, "A parallel algorithm for the computation of invariant tori in large-scale dissipative systems," Physica D **252**, 22–33 (2013).

[52] D. Rand, "Dynamics and symmetry. Predictions for modulated waves in rotating fluids," Arch. Ration. Mech. An. **79**, 1–37 (1982).

[53] P. S. Casas and À. Jorba, "Hopf bifurcations to quasi-periodic solutions for the two-dimensional plane Poiseuille flow," Commun. Nonlinear Sci. Numer. Simulat. **17**, 2864–2882 (2012).

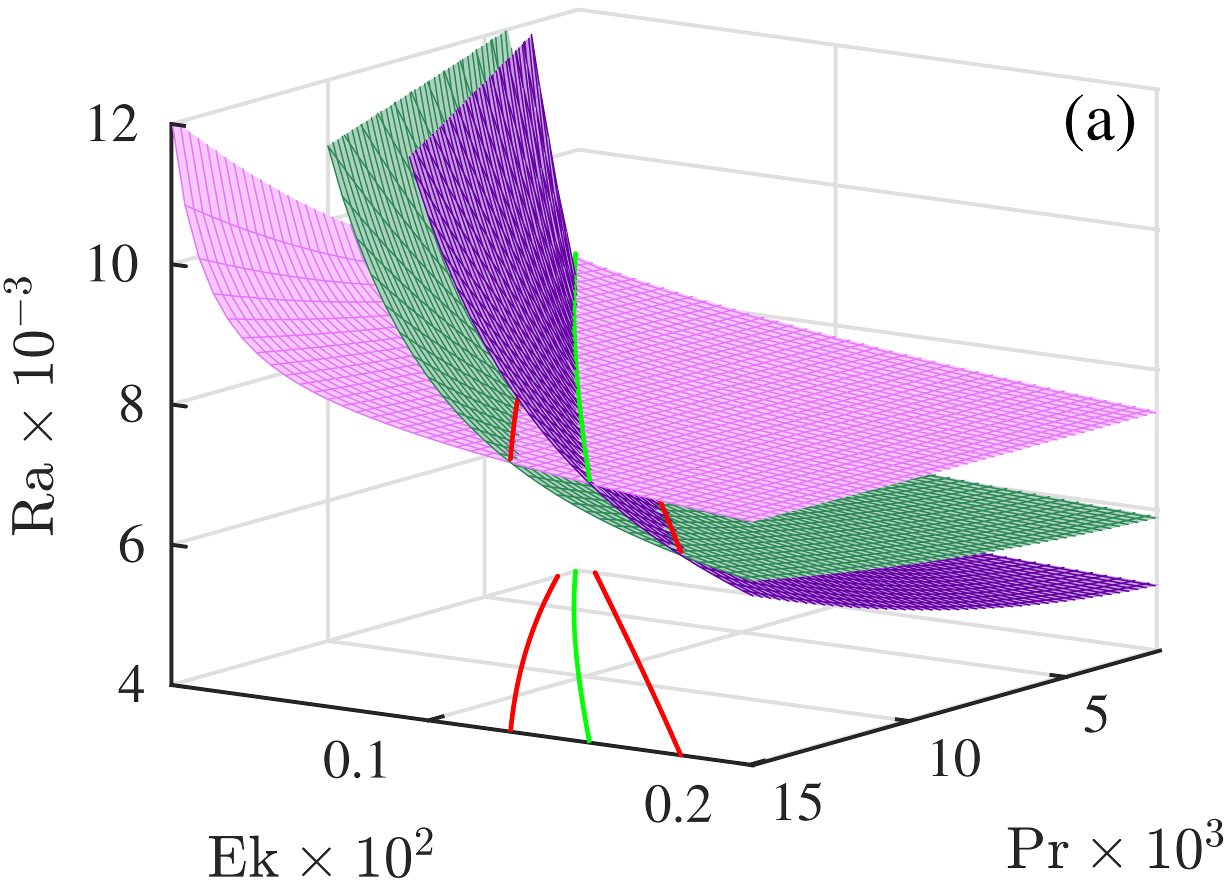
(a)
12
10
8
6
4
$\mathrm{Ra} \times 10^{-3}$
0.1
0.2
$\mathrm{Ek} \times 10^{2}$
15
10
5
$\mathrm{Pr} \times 10^{3}$

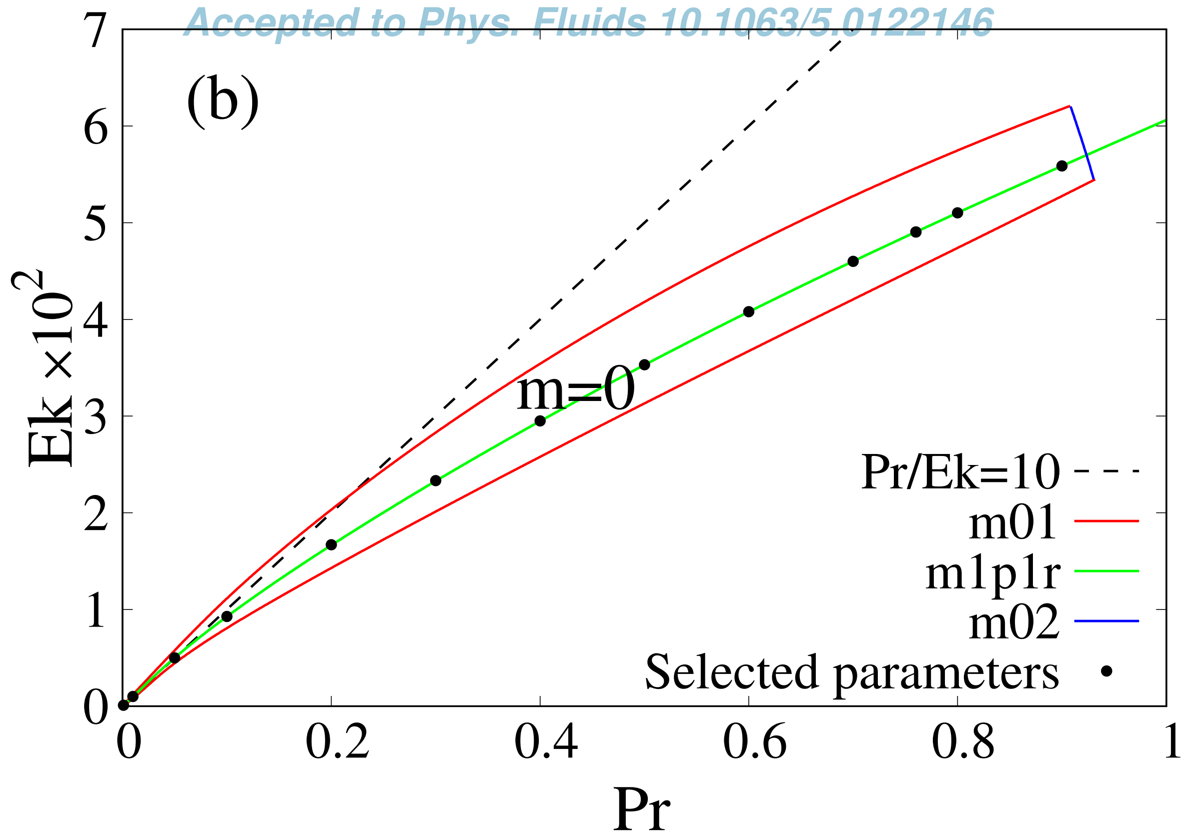
(b)
m=0
Pr/Ek=10
m01
m1p1r
m02
Selected parameters
Ek ×10^2
Pr
0
1
2
3
4
5
6
7
0.2
0.4
0.6
0.8

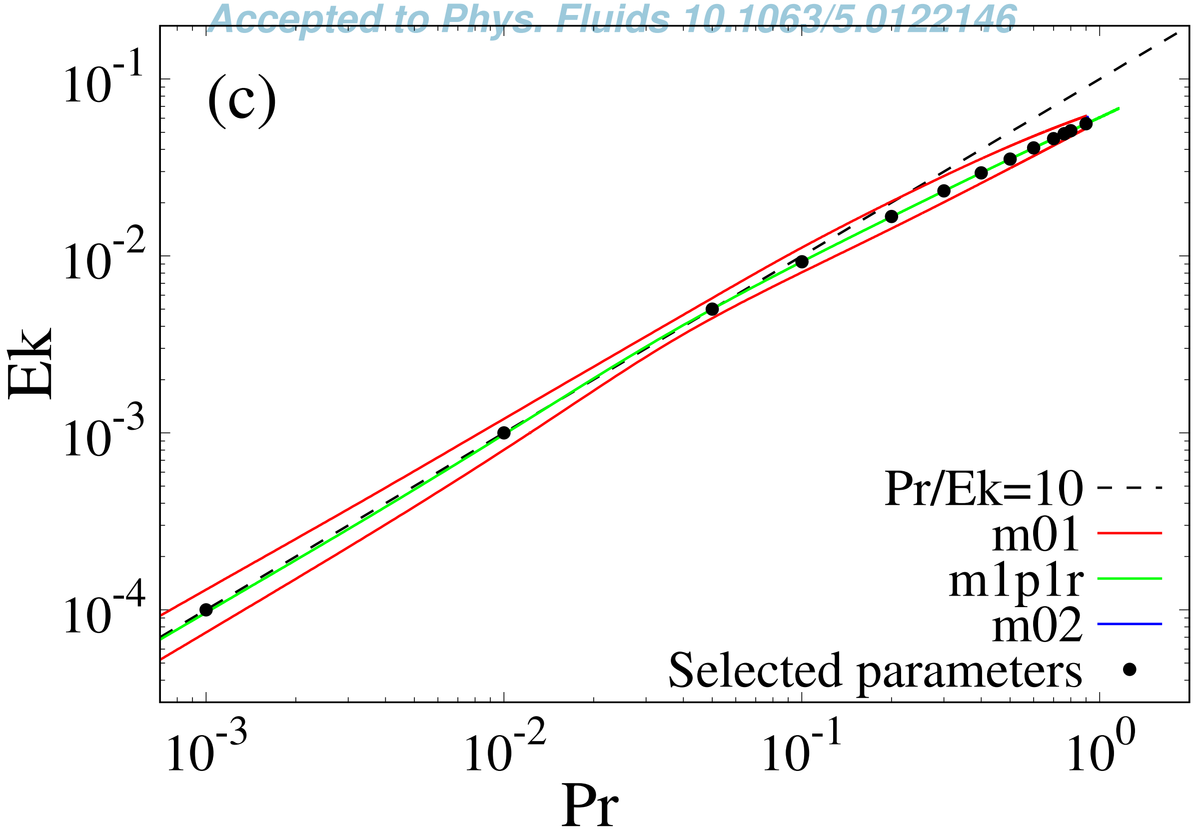
(c)
Ek
Pr
10^{-1}
10^{-2}
10^{-3}
10^{-4}
10^{-3}
10^{-2}
10^{-1}
10^{0}
Pr/Ek=10
m01
m1p1r
m02
Selected parameters

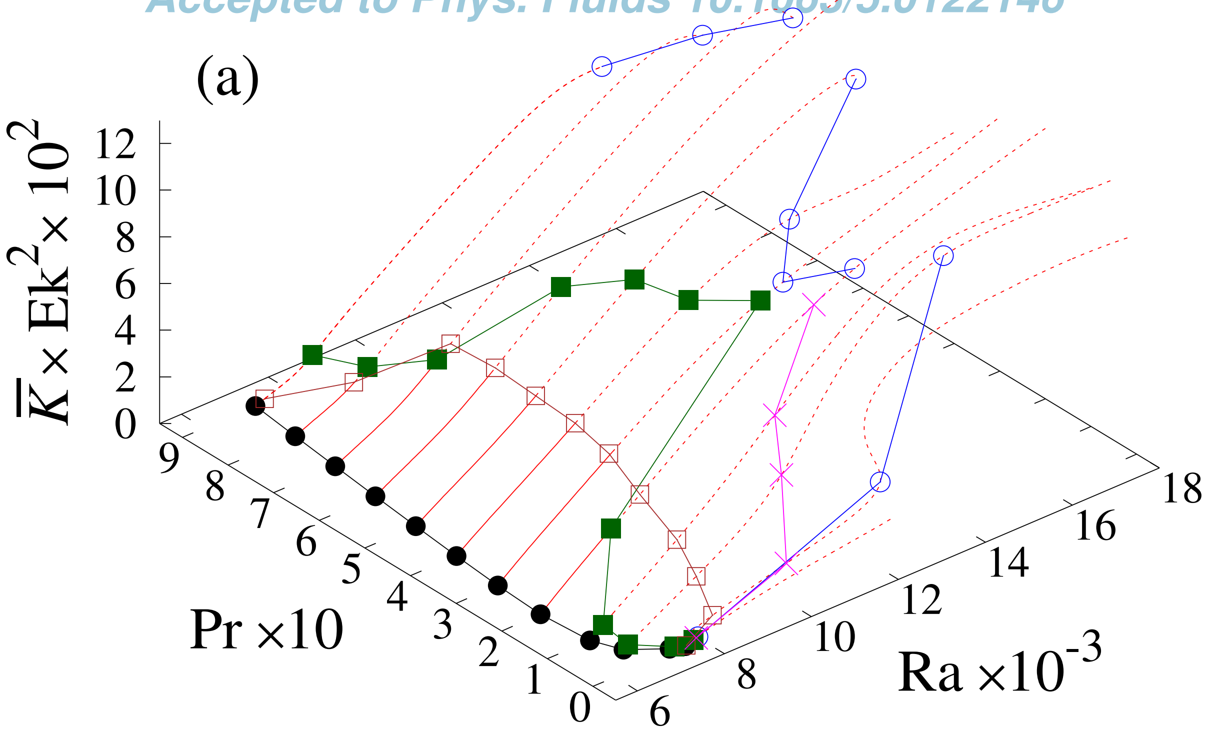
(a)
$\overline{K} \times \mathrm{Ek}^2 \times 10^2$
0
2
4
6
8
10
12
Pr ×10
0
1
2
3
4
5
6
7
8
9
Ra ×10^{-3}
6
8
10
12
14
16
18

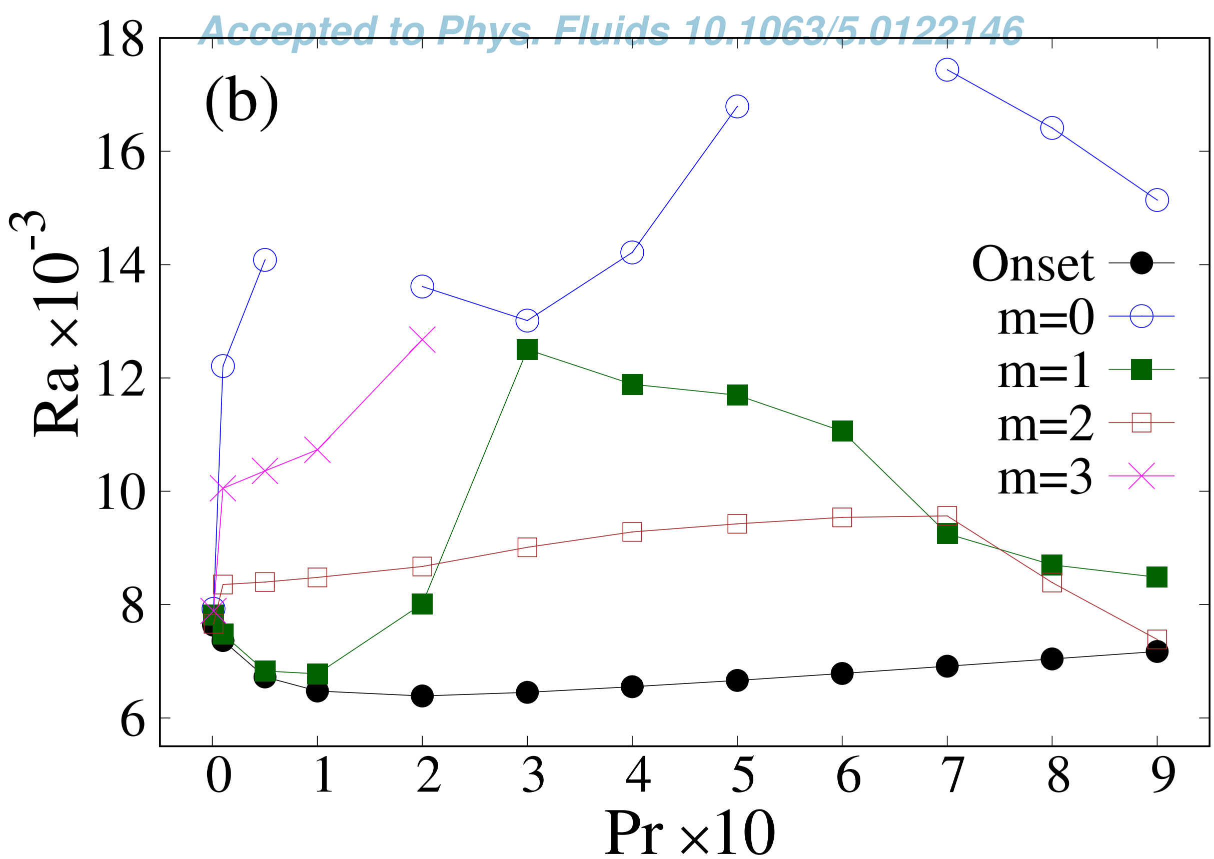
(b)
Onset
m=0
m=1
m=2
m=3
Ra ×10^{-3}
Pr ×10
6
8
10
12
14
16
18
0
1
2
3
4
5
6
7
8
9

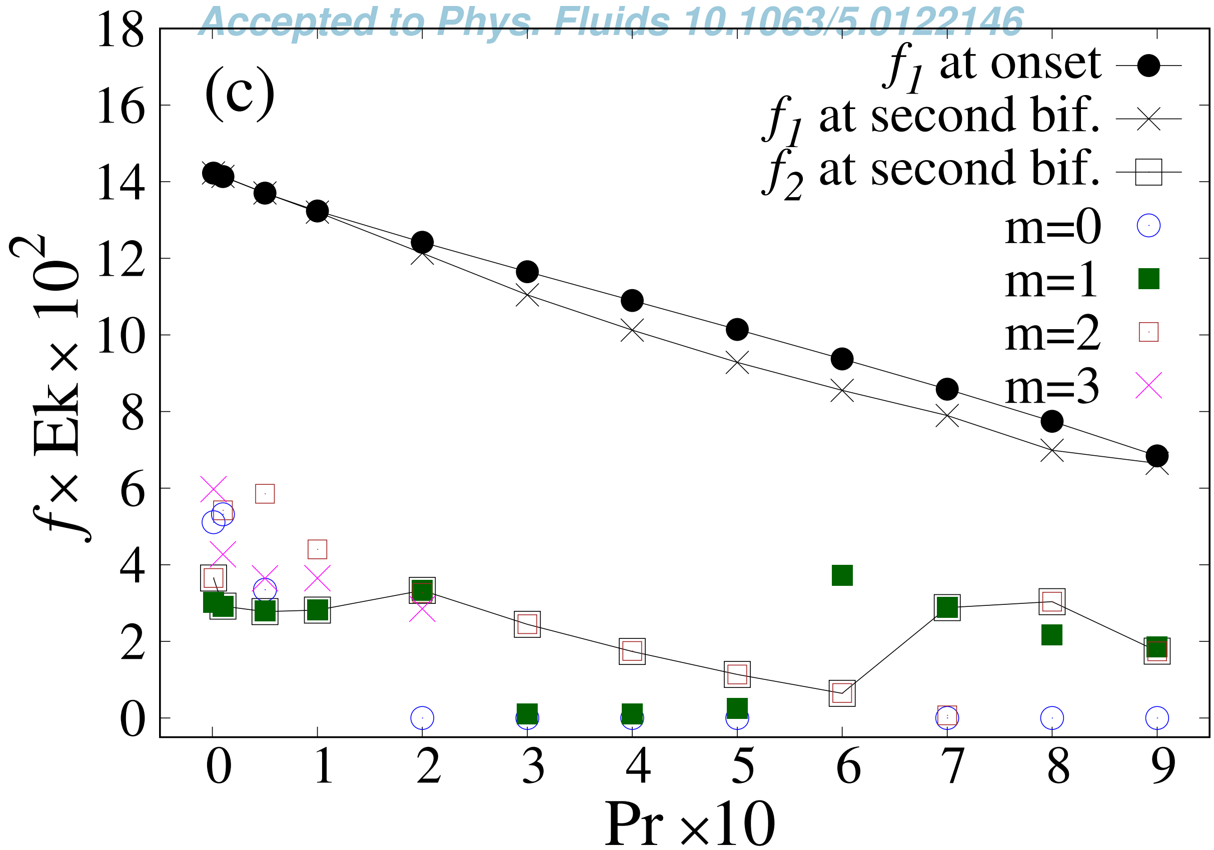
(c)
f_1 at onset
f_1 at second bif.
f_2 at second bif.
m=0
m=1
m=2
m=3
$f \times \mathrm{Ek} \times 10^2$
Pr ×10
0
2
4
6
8
10
12
14
16
18
0
1
2
3
4
5
6
7
8
9

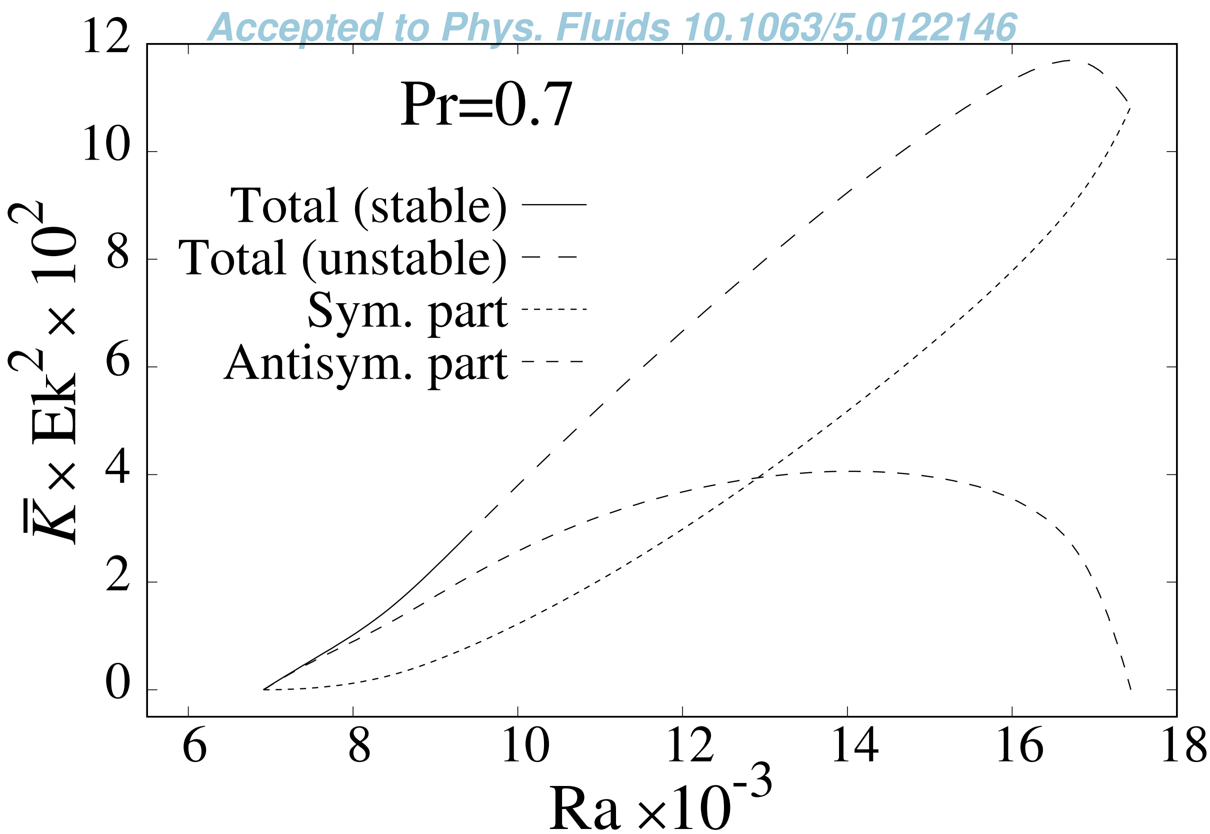
Pr=0.7
Total (stable)
Total (unstable)
Sym. part
Antisym. part
$\overline{K} \times \mathrm{Ek}^2 \times 10^2$
Ra $\times 10^{-3}$
0
2
4
6
8
10
12
6
8
10
12
14
16
18

Accepted to Phys. Fluids 10.1063/5.0122146

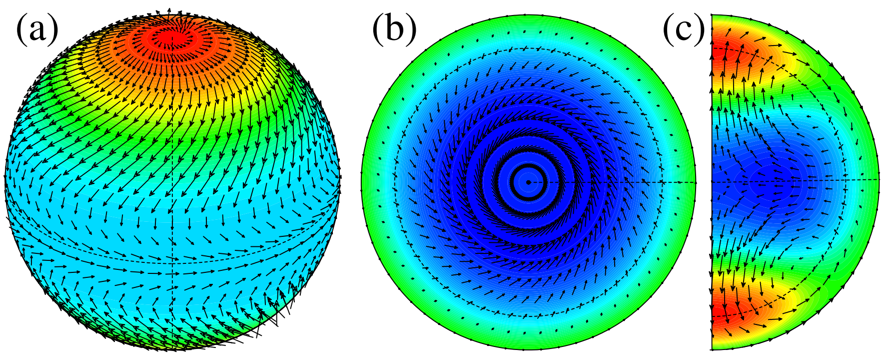

Accepted to Phys. Fluids 10.1063/5.0122146

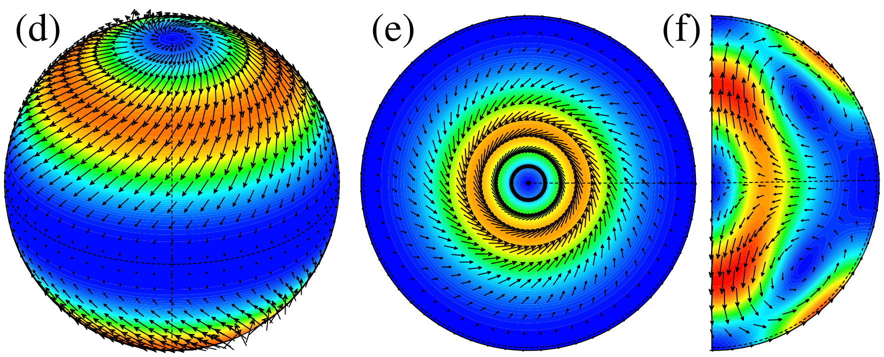

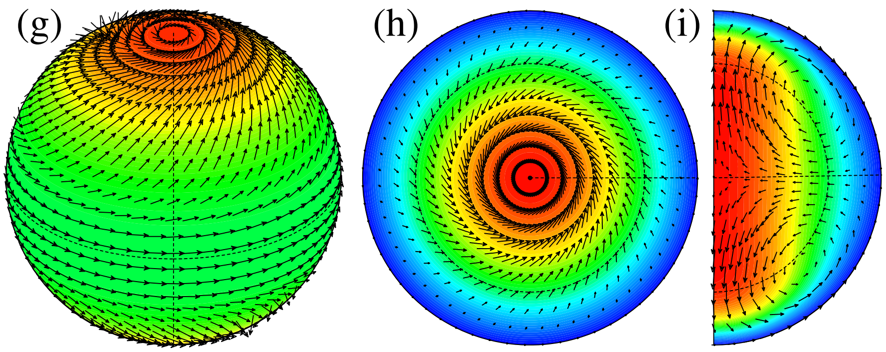
(g)
(h)
(i)

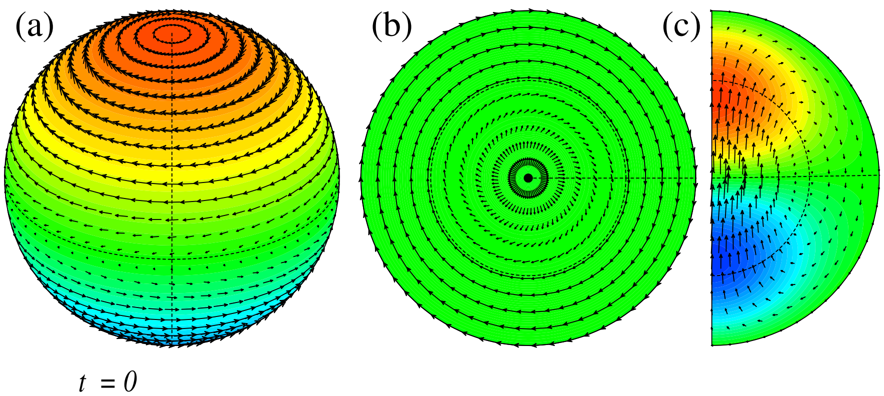
(a)
(b)
(c)
t = 0

Accepted to Phys. Fluids 10.1063/5.0122146

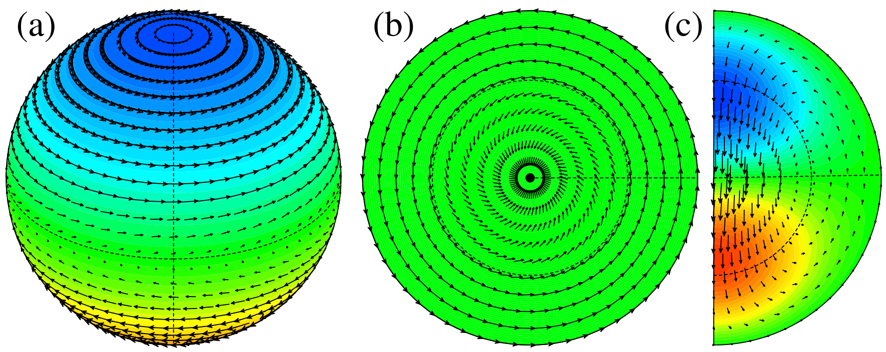

$t = T/2$

Accepted to Phys. Fluids 10.1063/5.0122146

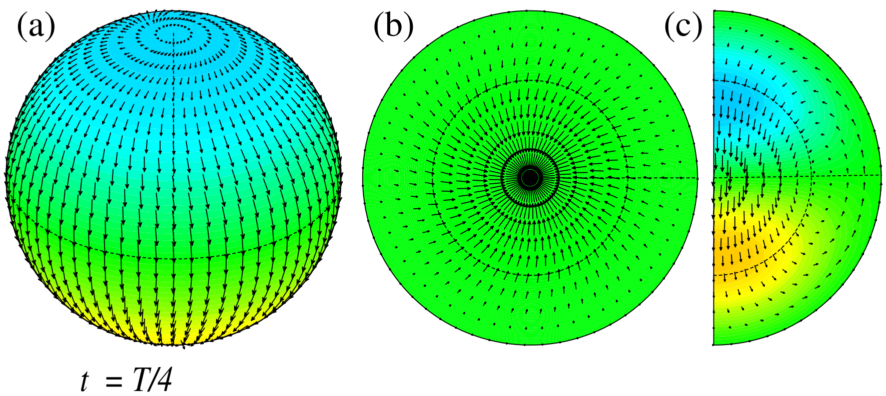

Accepted to Phys. Fluids 10.1063/5.0122146

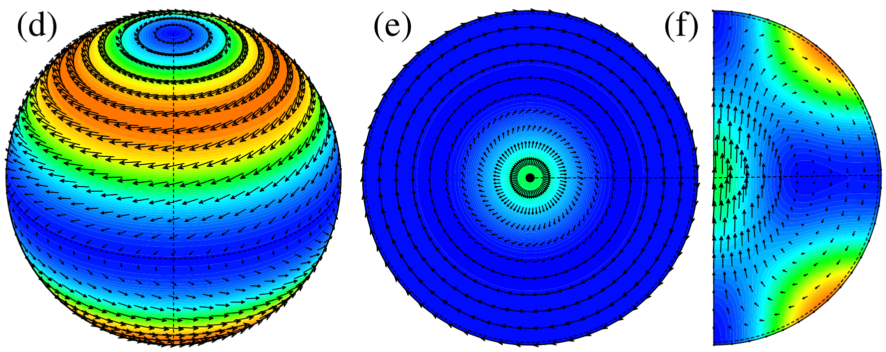

$t = 0$

Accepted to Phys. Fluids 10.1063/5.0122146

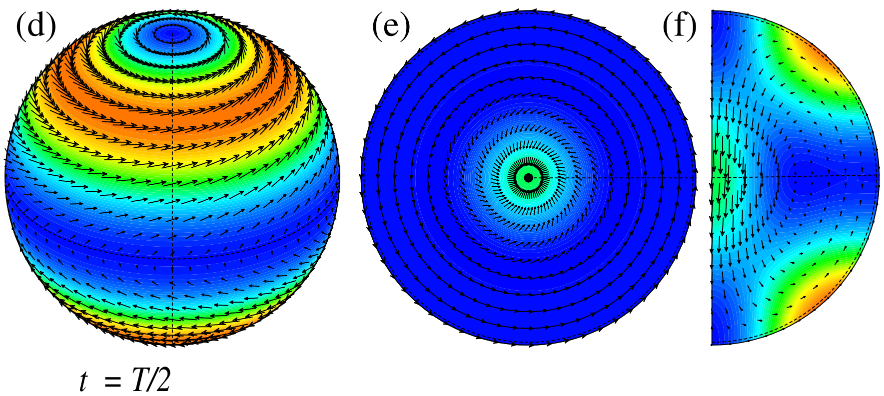

Accepted to Phys. Fluids 10.1063/5.0122146

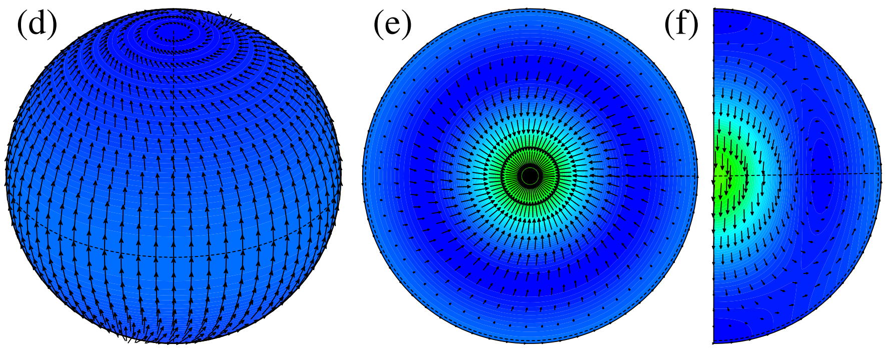

$t = T/4$

Accepted to Phys. Fluids 10.1063/5.0122146

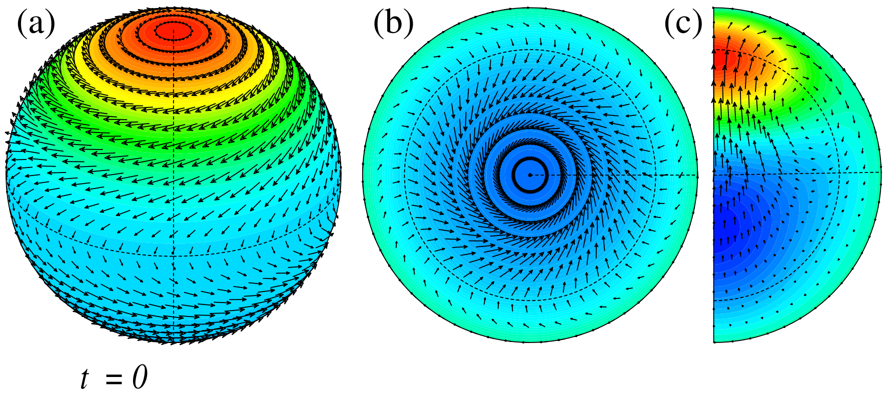

Accepted to Phys. Fluids 10.1063/5.0122146

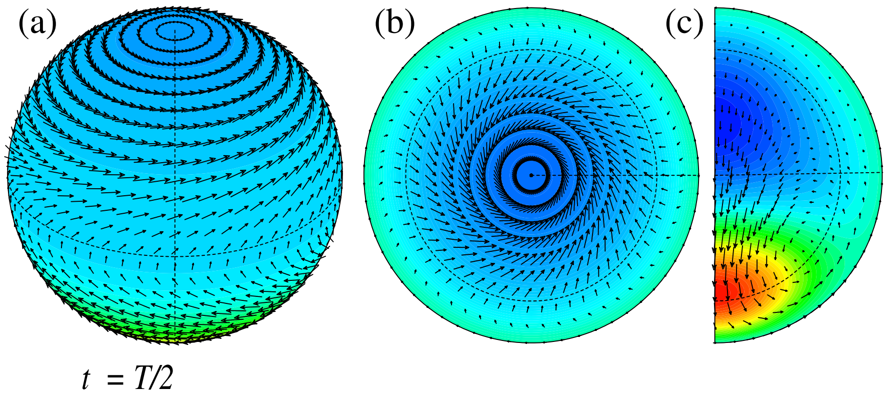

Accepted to Phys. Fluids 10.1063/5.0122146

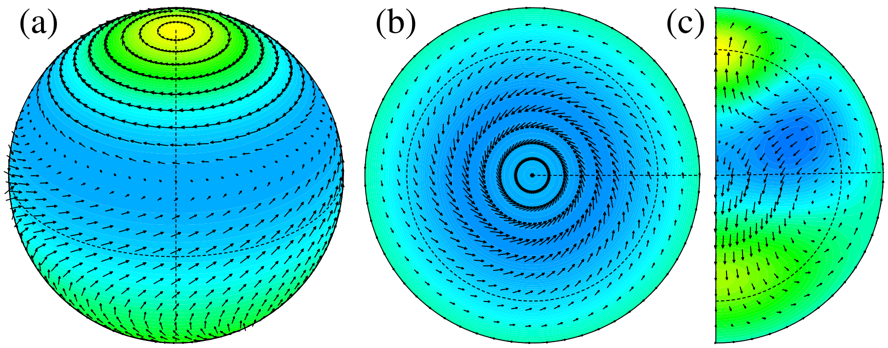

$t = T/4$

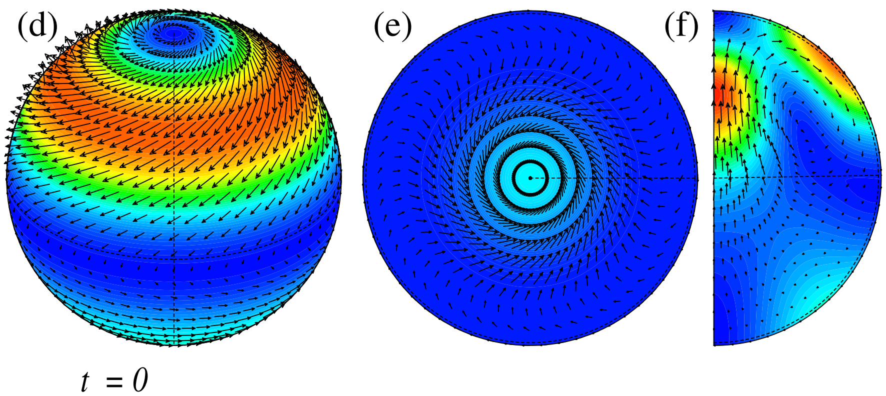
(d)
(e)
(f)
$t = 0$

Accepted to Phys. Fluids 10.1063/5.0122146

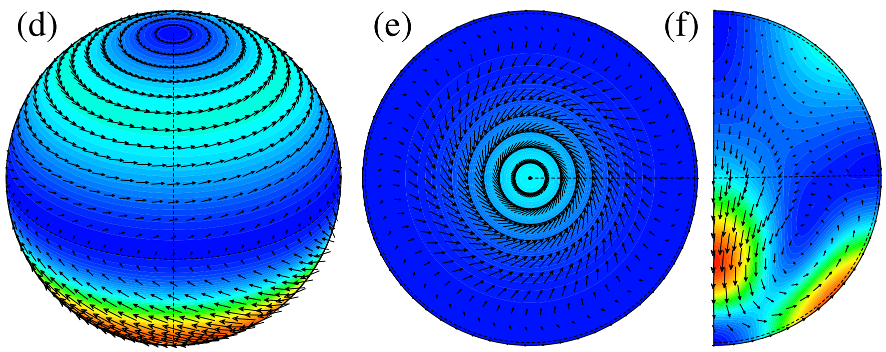

$t = T/2$

Accepted to Phys. Fluids 10.1063/5.0122146

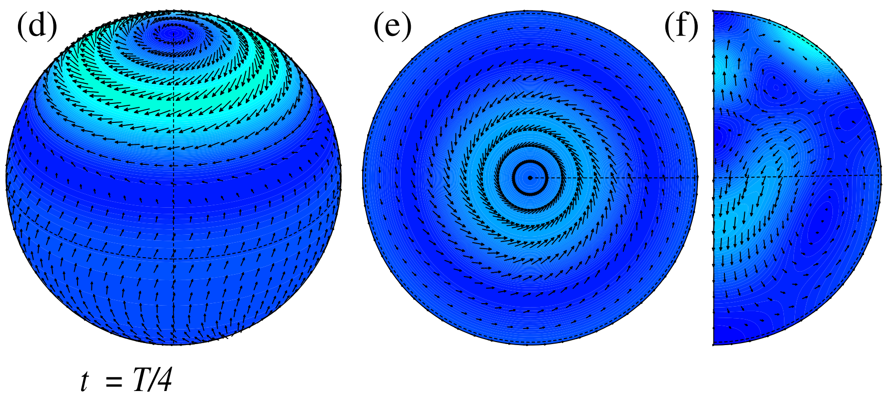

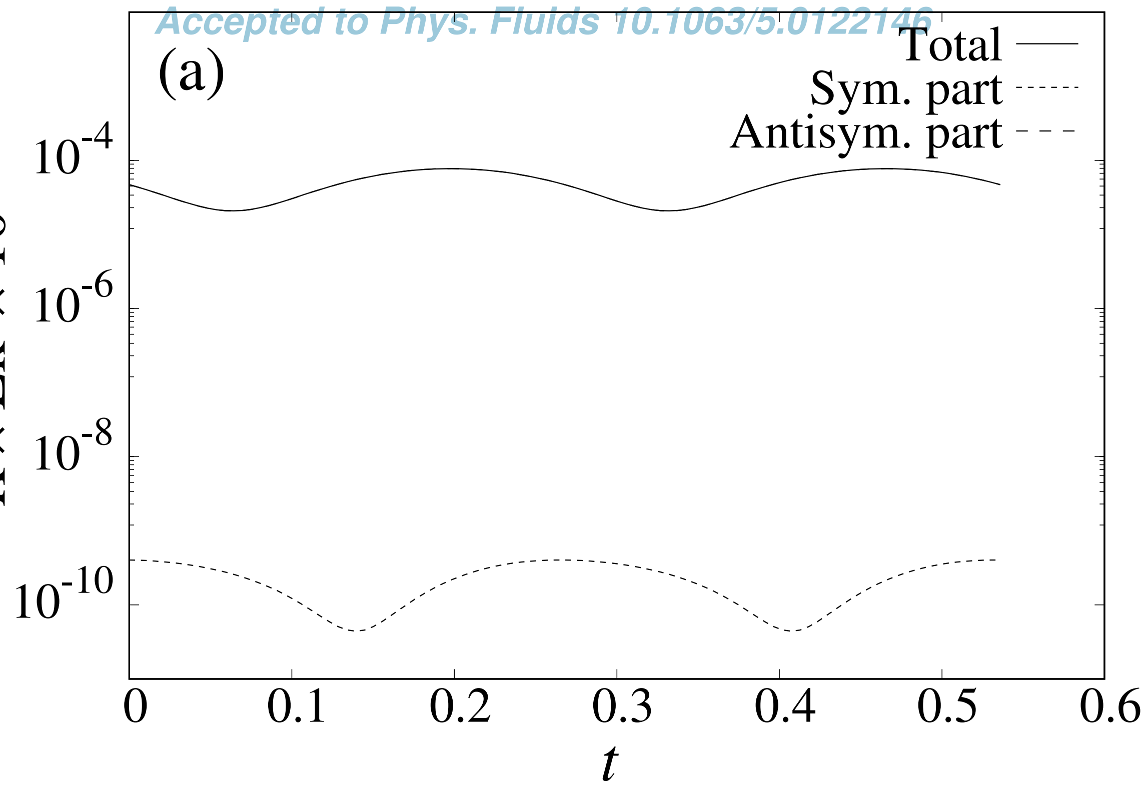
(a)
Total
Sym. part
Antisym. part
$K \times \mathrm{Ek}^2 \times 10^2$
10^{-4}
10^{-6}
10^{-8}
10^{-10}
0
0.1
0.2
0.3
0.4
0.5
0.6
t

Accepted to Phys. Fluids 10.1063/5.0122146

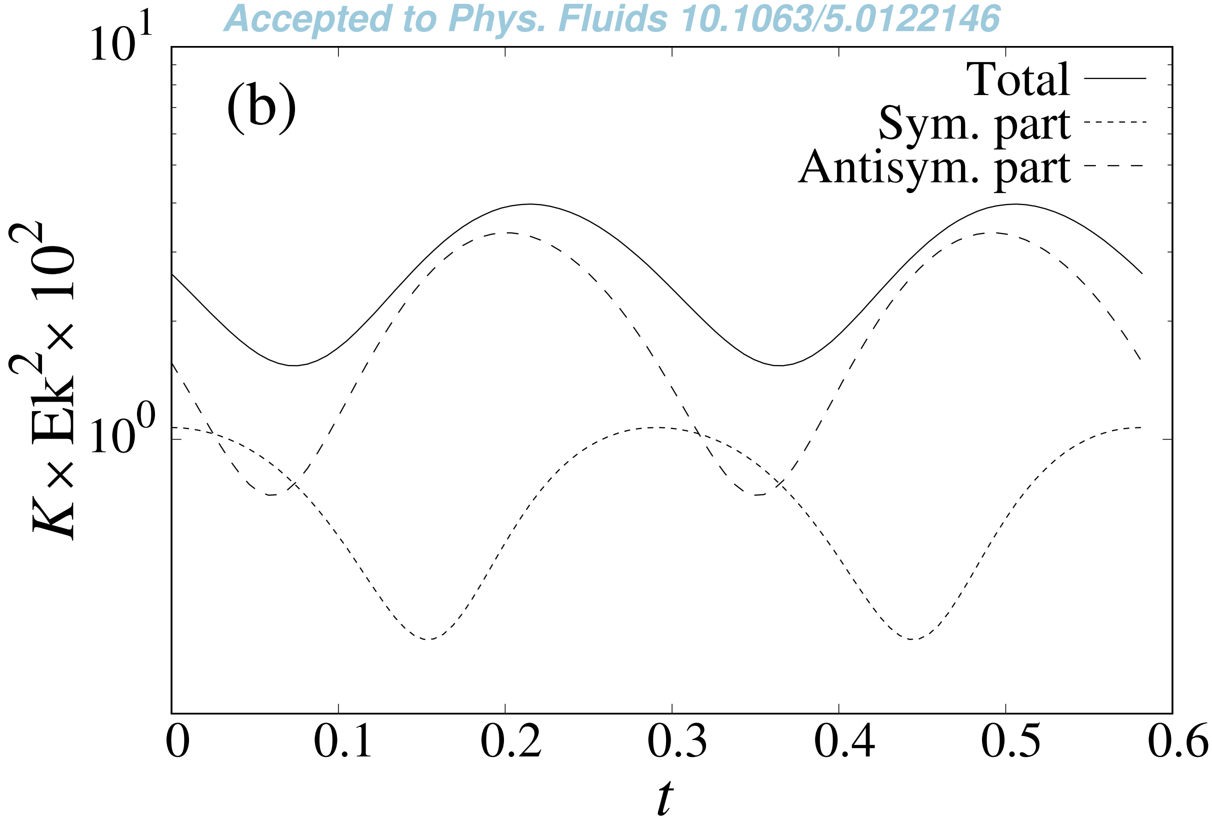

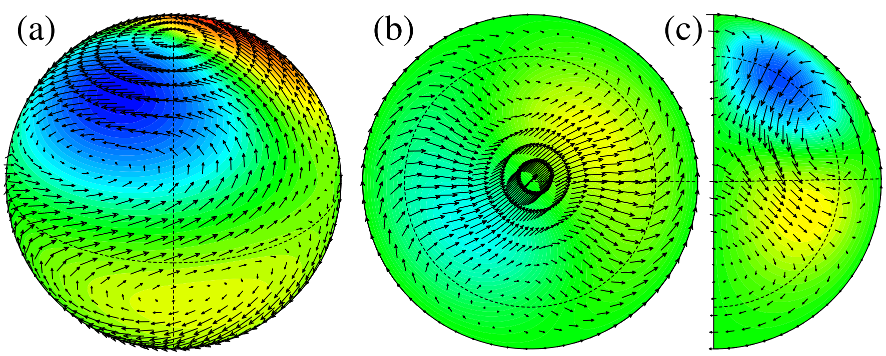

$t\ = 0$

Accepted to Phys. Fluids 10.1063/5.0122146

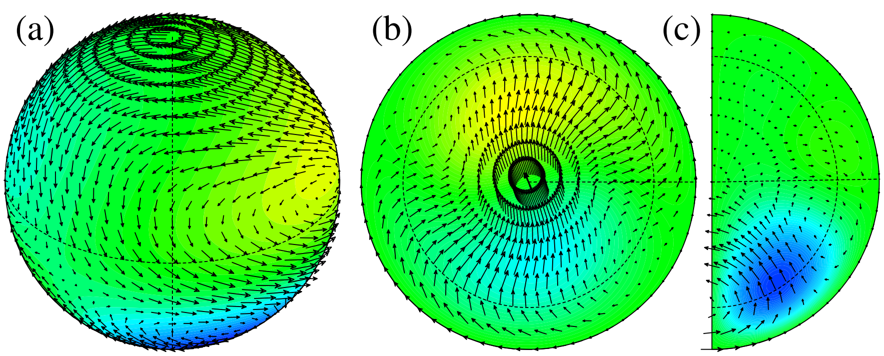

$t = T/2$

Accepted to Phys. Fluids 10.1063/5.0122146

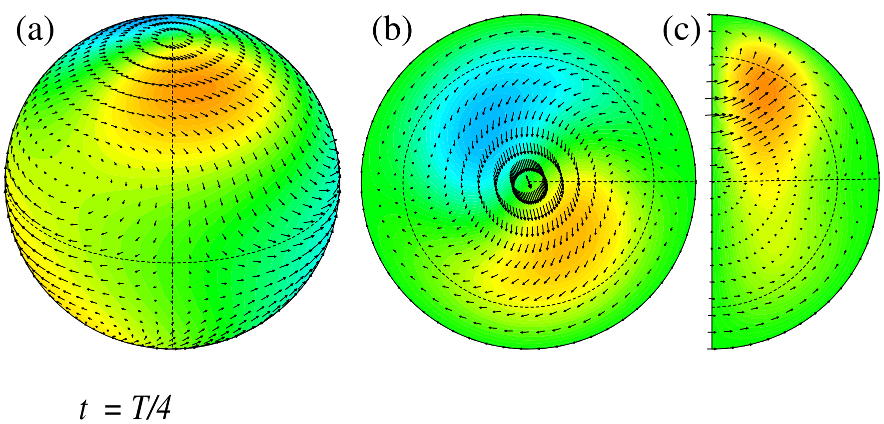

Accepted to Phys. Fluids 10.1063/5.0122146

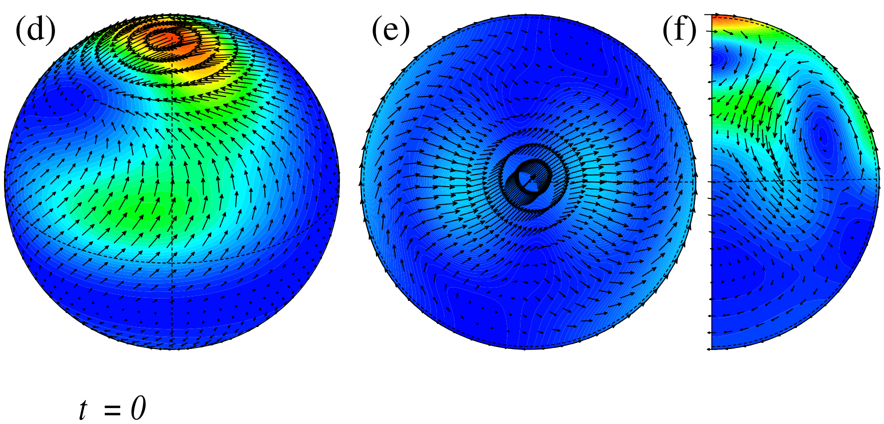

Accepted to Phys. Fluids 10.1063/5.0122146

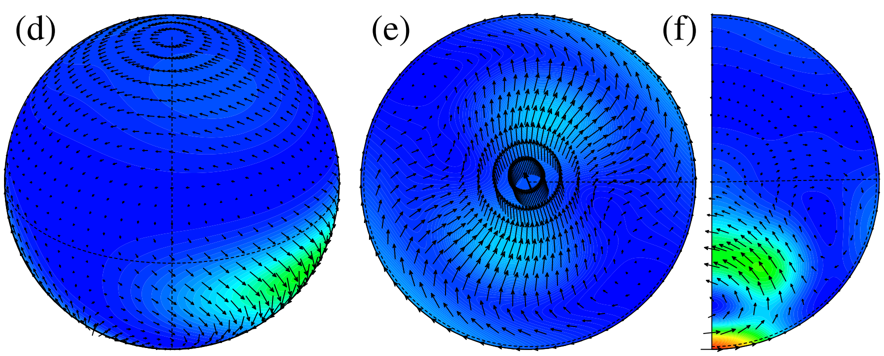

$t = T/2$

Accepted to Phys. Fluids 10.1063/5.0122146

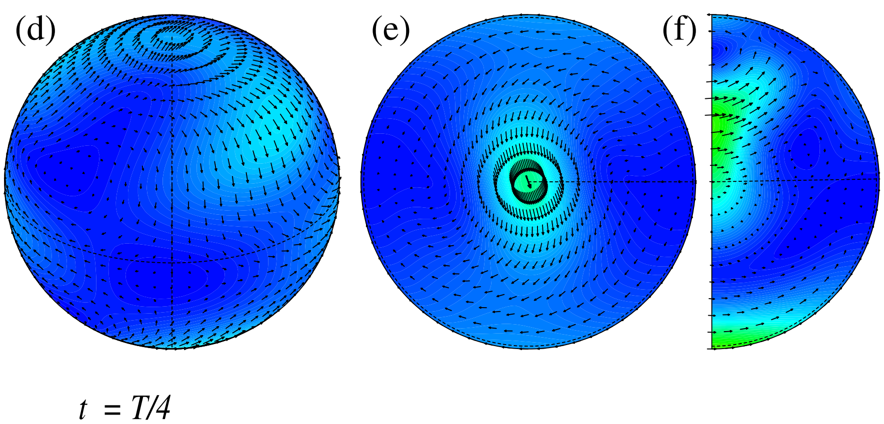

Accepted to Phys. Fluids 10.1063/5.0122146

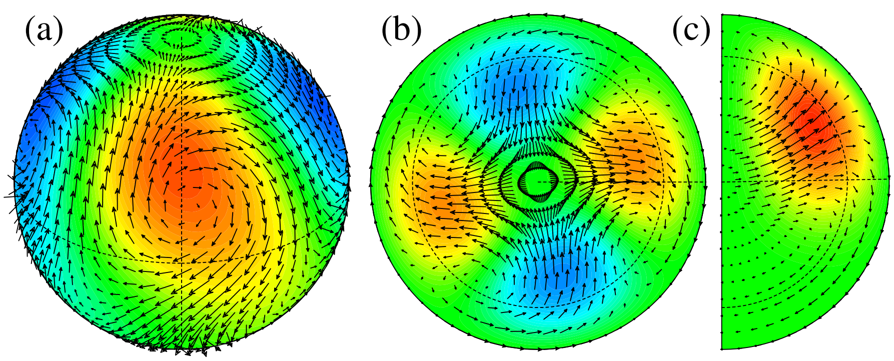

$t = 0$

Accepted to Phys. Fluids 10.1063/5.0122146

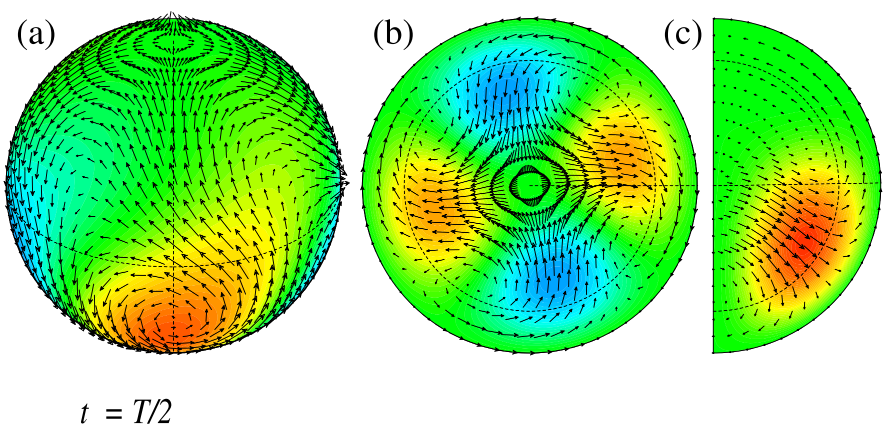

Accepted to Phys. Fluids 10.1063/5.0122146

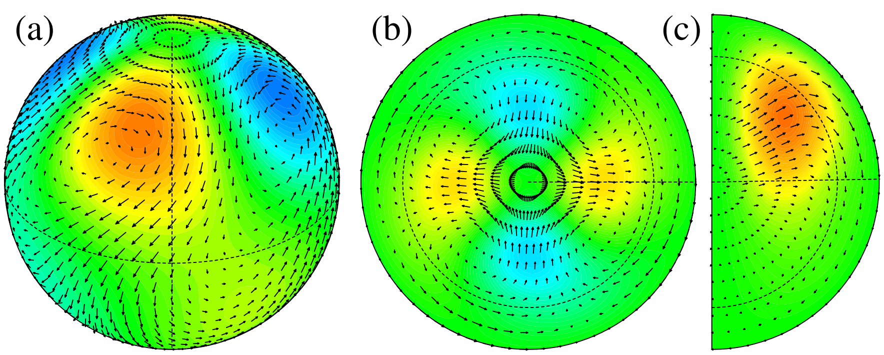

$t = T/4$

Accepted to Phys. Fluids 10.1063/5.0122146

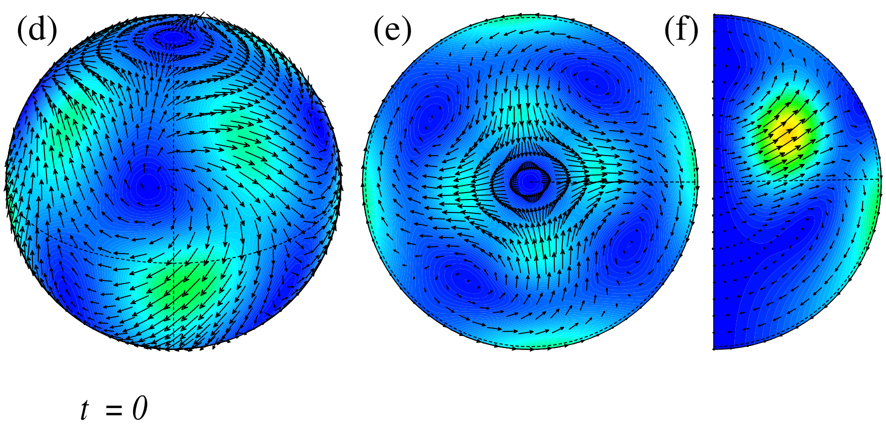

Accepted to Phys. Fluids 10.1063/5.0122146

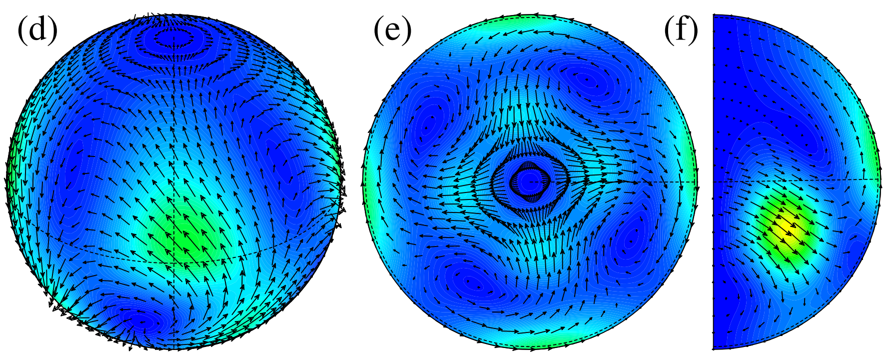

t = *T*/2

Accepted to Phys. Fluids 10.1063/5.0122146